Applied Ocean Research 168 (2026) 104984

Contents lists available at ScienceDirect

Applied Ocean Research

journal homepage: www.elsevier.com/locate/apor

Research paper

How depositional processes in turbidite deposits affect the self-acceleration of turbidity currents

Umberto Sasso [a,*], Gaetano Porcile [b], Octavio E. Sequeiros [c], Carlos Pirmez [b], Michele Bolla Pittaluga [a,b]

[a] Department of Civil, Chemical and Environmental Engineering, University of Genoa, Via Montallegro 1, Genoa, 16145, Italy
[b] Weather Water Sand S.r.l., Piazza della Vittoria, 14/19, Genoa, 16121, Italy
[c] Shell Global Solutions International B.V., Carel van Bylandtlaan 30, 2596 HR, The Hague, The Netherlands

ARTICLE INFO

Keywords:
Turbidity currents
Sediment density flow
Turbidite
Bed composition
RANS

ABSTRACT

This study investigates the conditions required for self-acceleration in laboratory-scale turbidity currents using a numerical model validated against experimental measurements. A series of simulations were conducted to isolate the main hydro-sedimentary factors potentially controlling the onset and sustenance of flow self-acceleration. Specific depositional processes, namely the vertical and lateral grain size composition of the turbidites formed by antecedent turbidity currents were found to affect the dynamics of subsequent flow events. Results show that simplified bed representations fail to reproduce self-accelerating regimes, demonstrating that an erodible bed is a necessary but not sufficient condition for a current to self-accelerate. In contrast, when the modelled bed exhibits realistic sedimentary features, such as bed slope increase due to cumulative deposition, downstream sediment fining, and vertical stratification, flows accelerate due to enhanced sediment entrainment. These findings underscore the critical role of past flow deposits in actively preconditioning the nature of future events.

1. Introduction

Turbidity currents are sediment-laden gravity flows in subaqueous environments, that represent the dominant mechanism for transporting sediment from shallow to deep waters. Turbidity currents can travel at high speeds and over great distances, posing hazards by scouring the sediment bed and damaging critical underwater infrastructures (Heezen and Ewing, 1952; Carter et al., 2009, 2014; Gavey et al., 2017; Pope et al., 2017; Porcile et al., 2020, 2023; Sequeiros et al., 2019). Along their flow paths, they continuously interact with the bed through erosion and/or deposition of sediments, and thus play a key role in the formation of deep-water geomorphological features (Kuenen and Migliorini, 1950; Heerema et al., 2020; Talling et al., 2022). Turbidity currents are also efficient carriers of organic matter from the continental shelf to the deep-sea, playing an important role in the global carbon cycle (Baker et al., 2024; Talling et al., 2023). For these reasons, their study is of critical importance in the fields of hydraulic engineering and marine geology.

The largest sediment accumulations on Earth are composed of turbidity current deposits, known as turbidites. These layered deposits are characterized by a vertically graded structure (Bouma, 1962; Lowe, 1982), typically featuring vertical stratification with a coarser sediment base and a finer-grained cap, reflecting the temporal deceleration of the flow at a specific location. Turbidites generally also exhibit downstream fining and thinning with their mean grain size and deposit thickness progressively decreasing due to the preferential transport/deposition of finer/coarser material and the spatial deceleration of the flow associated with a decrease in gradient towards the deeper basin. These distinctive vertical and downflow grain-size trends of turbidites have important implications for geologic records and hydrocarbon reservoirs (Mutti, 1985; Weimer and Link, 1991; Normark and Piper, 1991).

A defining feature of turbidity currents is their ability to exchange sediment with the bed, creating a feedback mechanism that strongly influences the current behaviour (Pantin, 1979). If the flow loses more sediment through deposition than it gains through erosion, it will gradually decelerate and eventually dissipate as its excess density relative to the ambient fluid decreases. When erosion and deposition rates are in equilibrium, the turbidity current attains an auto-suspending state in which velocity and sediment load reach a quasi-steady condition. In this auto-suspensive regime (also called bypassing), the net sediment exchange between the flow and the bed approaches zero. However, rather than being a static condition, the persistence of such flows over

* Corresponding author.
E-mail address: umberto.sasso@edu.unige.it (U. Sasso).

https://doi.org/10.1016/j.apor.2026.104984
Received 17 September 2025; Received in revised form 20 January 2026; Accepted 16 February 2026
Available online 23 February 2026

long distances is maintained by complex dynamic processes (Ma et al., 2025; Salinas et al., 2020). If the turbidity current entrains sediment from the bed faster than it deposits, its excess density increases, causing the flow to accelerate downslope. The onset of this process is known as ignition, which triggers a self-reinforcing feedback loop: greater erosion leads to a denser, faster flow, which in turn enhances further erosion. This sustained state is commonly referred to as self-acceleration (Parker et al., 1986). Notably, the availability of erodible bed sediment has been identified as a critical factor: a turbidity current can only become self-accelerating if sufficient loose sediment is present on the seabed to fuel it (Parker, 1982). Parker (1982) also suggested that it is easy to envision a self-sustaining turbidity current composed mostly of fine sediment, as its low settling velocity enables it to remain in suspension and continue driving the flow (Salaheldin et al., 2000). In other words, a finer suspended load should make it easier for a flow to sustain itself. These concepts imply that the nature of the bed material (such as its mean grain size and erodibility) influences whether a given flow will ignite into a self-sustaining erosive current or deposit its load and dissipate (Stacey and Bowen, 1988). Despite this sound theoretical framework, direct observation and reproduction of self-accelerating turbidity currents have historically been challenging. Only a few field observations and laboratory experiments have succeeded in assessing the occurrence of such complex hydro-sedimentary processes.

Field observations of turbidity currents are very challenging, as these events are episodic and typically occur at great water depths, making direct measurements rare. Consequently, earlier assessments of turbidity current dynamics often relied solely on indirect observations — for example, inferring flow behaviour from deposit grain-size trends or erosion marks (Sumner et al., 2008; Inman et al., 1976; Prior et al., 1987; Normark et al., 1989; Garfield et al., 1994; Xu et al., 2004). Such geological analyses have led to valuable classifications of turbidity currents as either erosional or depositional flows (Sylvester and Lowe, 2004; Normark and Piper, 1991). However, they could not directly capture how the flow-bed interactions evolved in real-time. Advanced in-situ monitoring has only recently begun to directly observe the dynamics of both the flow and the bed (Liu et al., 2012; Cooper et al., 2016; Hughes Clarke, 2016; Paull et al., 2018; Normandeau et al., 2020). In particular, detailed measurements of turbidity currents in the sand-rich Monterey Canyon have shown that faster flows initially entrain sediment and maintain nearly uniform velocities, while slower flows dissipate rapidly (Heerema et al., 2020). Notably, one exceptional flow observed in this system self-accelerated in the mid-canyon and was attributed to the erosion of an unusually erodible layer of fine sediment. This highlighted that the evolution of turbidity currents is highly sensitive to the grain size of the bed sediment they encounter. In line with these findings, field observations in the mud-rich Congo Canyon have directly recorded subsequent turbidity currents accelerating downslope. One flood-triggered flow was observed to increase in velocity from about 5.2 to 8.0 m/s while travelling over 1100 km and leaving meter-deep erosional signatures, confirming that strongly erosional flows can self-accelerate and travel exceptionally far (Talling et al., 2022). These recent insights underscore the occurrence of self-acceleration in the field and indicate that finer-grained flows travel much farther than coarser-grained flows (Azpiroz-Zabala et al., 2017). However, the underlying processes controlling these types of flows remain under debate, and a clear quantification of the impact of sediment composition on turbidity current self-acceleration is still lacking.

Reproducing self-acceleration under controlled laboratory conditions has also proven to be challenging. Previous experiments involving turbidity currents flowing over erodible beds failed to capture the onset of self-acceleration: the experimental flows typically deposited sediment and slowed down before acceleration could occur. For example, Parker et al. (1987) conducted flume experiments specifically designed to investigate this process, but they did not observe any sign of self-acceleration. Nonetheless, laboratory experiments have proven effective in revealing specific interactions between turbidity currents and the bed sediment. Using a poorly sorted sediment mixture, Garcia (1994) observed that both sediment deposition rates and the grain size of the resulting deposits decreased consistently with distance from the sediment source, demonstrating that turbidites can indeed be reproduced in the laboratory. Additionally, experiments by Gladstone et al. (1998) showed that adding fine sediment to a coarse-grained gravity current significantly increased flow velocities and run-out distances, highlighting the importance of sediment grain-size distribution within the flow. More recently, Eggenhuisen et al. (2020) explored how turbulence within turbidity currents drives vertical grain-size segregation: coarser grains tend to concentrate near the base of the flow, while finer particles remain suspended in the upper layers. A major breakthrough was finally achieved by the experiments of Sequeiros et al. (2018), who reported the first direct observation of self-acceleration in a laboratory setting.

Building on earlier experimental efforts (Sequeiros et al., 2009, 2010), Sequeiros et al. (2018) conducted a series of flume experiments that successfully reproduced self-accelerating turbidity currents. Two key innovations enabled them to replicate a field-like scenario that had long been hypothesized in theoretical models. First, they introduced mixtures of water and sediments via a surface diffuser, rather than injecting it directly near the sediment bed, which caused the hyperpycnal plunging of the dense inflows that formed downslope supercritical turbidity currents. The plunging mechanism purged the inlet flow of excess sediment, which settled upstream of the plunging point, allowing the downstream development of turbidity currents that were not over capacity. Second, they released multiple successive turbidity currents in the same flume setup, so that each current inherited an erodible bed composed of deposits from preceding flows. This approach avoided the artificial use of well-mixed, freshly-prepared beds and instead mimicked natural conditions, where turbidity currents often traverse the deposits left by earlier events. As a result, their experiments provided the first laboratory realization of self-accelerating turbidity currents evolving over realistic turbidite beds, bridging the gap between simplified experimental setups and the complex nature of subaqueous systems. Despite this achievement, the underlying processes governing the onset of self-acceleration remained unclear. Only under certain conditions did the experimental flows display self-acceleration. The authors suggested that factors such as inlet flow discharge, initial sediment concentration, cumulative changes in bed slope due to deposition, and the availability of easily entrainable sediment along the bed may have contributed to the emergence of self-acceleration.

Recent advances in numerical modelling have expanded the available approaches for simulating turbidity currents, including particle-resolving CFD-DEM methods that capture particle-scale dynamics (Lu et al., 2024a), mesh-free techniques such as the Consistent Particle Method (Tang et al., 2023), and hybrid deep learning-CFD frameworks for turbidity current forecasting (Fazel Mojtahedi et al., 2025). Additionally, process-based numerical models are increasingly applied to investigate flow responses to realistic submarine topographies (Lu et al., 2024b; Sequeiros et al., 2019; Frascati et al., 2025). However, none of these studies have explicitly examined how the sedimentary structure of turbidite deposits influences the onset and sustenance of self-acceleration.

In this study, we replicate and extend the experiments of Sequeiros et al. (2018) using a digital twin of their flume setup, based on the Reynolds-averaged Navier–Stokes (RANS) modelling framework developed by Porcile et al. (2022). By simulating successive turbidity currents and their associated deposits, we systematically isolate the depositional processes potentially responsible for self-acceleration, evaluating their individual contributions to its onset and sustenance.

The remainder of this manuscript is organized as follows: The Methods section describes the numerical setup in detail, with particular emphasis on the modelling of sediment transport processes. The Results section presents the simulated flow dynamics, focusing on the effects of increasing bed slope, downstream fining and vertical stratification

of the bed sediment, on the downslope evolution of turbidity currents and their resulting deposits. The Discussion section synthesizes the key findings, highlighting the role of bed composition in governing the onset and sustenance of turbidity current self-acceleration. Finally, the Conclusions section summarizes the main outcomes of the study.

2. Methods

Numerical modelling of turbidity current hydrodynamics and their morphodynamic interactions with the bed is performed using Delft3D-Flow, a state-of-the-art software capable of simulating a wide range of hydro-sedimentary processes in both fluvial and marine environments (Deltares, 2025). Porcile et al. (2022) developed two applications of Delft3D to reproduce the hydrodynamics of experimental density (saline) and turbidity currents described by Sequeiros et al. (2009, 2010, 2018). Specifically, Porcile et al. (2022) were able to replicate laboratory-scale turbidity underflows using both the hydrostatic and non-hydrostatic versions of the software.

Modelled velocities and excess densities produced by both versions compared well with measured values in the upstream section of the flume. However, the models failed to capture the dynamics of the self-accelerating currents observed by Sequeiros et al. (2018) in the central and downstream sections of the flume. This limitation was attributed to the absence of feedback between the flow and the sediment bed in the model. Although the non-hydrostatic version of Delft3D provides a better representation of turbidity currents where strong density gradients occur, particularly their fronts, it currently only solves the hydrodynamics and does not incorporate sediment transport processes and morphological evolution capable of simulating the erosion and deposition of stratified beds, which were therefore neglected in that study.

In this study, we extend the hydrostatic modelling approach of Porcile et al. (2022) by incorporating both sediment transport and morphodynamic processes that control stratified bed composition during the occurrence of turbidity currents. This allows us to simulate successive turbidity current events and their associated deposits, as reported by Sequeiros et al. (2018), and to evaluate the contribution of depositional and erosional processes to the self-acceleration mechanism.

2.1. Hydrodynamics

Hydrodynamics is modelled by solving the Reynolds-Averaged Navier–Stokes (RANS) equations over a two-dimensional over the vertical (2DV) domain. This approach captures both horizontal and vertical flow dynamics while assuming uniformity in the transverse direction, making it suitable for simulating turbidity currents in a straight channel or flume. A horizontal Cartesian coordinate system is used in combination with a terrain-following sigma-coordinate system (σ) in the vertical, where σ is defined as the normalized vertical position along the direction of gravity, ranging from $\sigma = 0$ at the free surface to $\sigma = -1$ at the bed.

The continuity equation, which ensures mass conservation, is expressed in the σ-coordinate system as:

$$\frac{\partial \zeta}{\partial t} + \frac{\partial (hu)}{\partial x} + \frac{\partial \omega}{\partial \sigma} = hQ \,, \tag{1}$$

where ζ is the free surface elevation above the reference plane (at $z = 0$), t is time, h is the total water depth, u is the horizontal velocity in the x-direction, x is the horizontal coordinate, ω is the vertical velocity in the σ-coordinate system, and Q represents water inflow or outflow due to discharge or withdrawal. It is important to note that the vertical velocity in Cartesian coordinates, w, is not directly computed during the simulation. Instead, it is derived from the continuity equation, which allows the model to avoid its explicit calculation.

The horizontal momentum equation is expressed as:

$$\frac{\partial u}{\partial t} + u\frac{\partial u}{\partial x} + \frac{\omega}{h}\frac{\partial u}{\partial \sigma} = -\frac{1}{\rho}\frac{\partial p}{\partial x} + \frac{\partial}{\partial x}\left(2\nu_H\left(\frac{\partial u}{\partial x} + \frac{\partial u}{\partial \sigma}\frac{\partial \sigma}{\partial x}\right)\right) + \frac{1}{h^2}\frac{\partial}{\partial \sigma}\left(\nu_V\frac{\partial u}{\partial \sigma}\right) + M_x \,, \tag{2}$$

where ρ is the fluid density, $\frac{\partial p}{\partial x}$ is the horizontal pressure gradient, ν_H and ν_V are respectively the horizontal and vertical eddy viscosity coefficients, and M_x represents momentum contributions from external sources or sinks (e.g., water discharge or withdrawal).

The vertical momentum equation is reduced to the hydrostatic pressure approximation:

$$\frac{\partial p}{\partial \sigma} = -\rho g h \,, \tag{3}$$

where g is the gravitational acceleration. The horizontal pressure gradient accounts for both surface elevation changes and density variations due to sediment concentration, and is expressed as:

$$\frac{\partial p}{\partial x} = \rho_w g\frac{\partial \zeta}{\partial x} + gh\int_0^{\sigma}\left(\frac{\partial \rho}{\partial x} + \frac{\partial \rho}{\partial \sigma}\frac{\partial \sigma}{\partial x}\right)d\sigma' \,, \tag{4}$$

where ρ_w is the reference water density. Density variations are modelled as a function of the suspended sediment concentration c, which accounts for contributions from multiple sediment fractions:

$$\rho = \rho_w + \sum_{n=1}^{N} c^{(n)}\left(1 - \frac{\rho_w}{\rho_s^{(n)}}\right) \,, \tag{5}$$

where $\rho_s^{(n)}$ is the specific density of sediment fraction n, and N is the total number of sediment fractions.

Reynolds stresses are modelled using the Boussinesq approximation, with a constant horizontal eddy viscosity which accounts for sub-grid scale turbulence, and a vertical eddy viscosity that varies in both space and time. The vertical eddy viscosity is parameterized using the k–ϵ turbulence closure model, which has been shown to properly reproduce the vertical structure of laboratory and field scale turbidity currents (Choi and García, 2002; Huang et al., 2005, 2007). The model solves two transport equations for the turbulent kinetic energy (k) and its dissipation rate (ϵ):

$$\frac{\partial k}{\partial t} + u\frac{\partial k}{\partial x} + \frac{\omega}{h}\frac{\partial k}{\partial \sigma} = \frac{1}{h^2}\frac{\partial}{\partial \sigma}\left(\frac{\nu_V}{\sigma_k}\frac{\partial k}{\partial \sigma}\right) + P + B - \epsilon \,, \tag{6}$$

$$\frac{\partial \epsilon}{\partial t} + u\frac{\partial \epsilon}{\partial x} + \frac{\omega}{h}\frac{\partial \epsilon}{\partial \sigma} = \frac{1}{h^2}\frac{\partial}{\partial \sigma}\left(\frac{\nu_V}{\sigma_\epsilon}\frac{\partial \epsilon}{\partial \sigma}\right) + \frac{\epsilon}{k}\left[c_{1\epsilon}P + c_{1\epsilon}(1 - c_{3\epsilon})B - c_{2\epsilon}\epsilon\right] \,, \tag{7}$$

where P is the turbulence production due to shear, B is the buoyancy production term, and σ_k, σ_ϵ, $c_{1\epsilon}$, $c_{2\epsilon}$, and $c_{3\epsilon}$ are empirical constants. Standard values are adopted: $c_{1\epsilon} = 1.44$, $c_{2\epsilon} = 1.92$, $c_{3\epsilon} = 0$ (to suppress buoyancy damping for density currents), $\sigma_k = 1.0$, and $\sigma_\epsilon = 1.3$. The vertical eddy viscosity is then computed as:

$$\nu_V = c_\mu\frac{k^2}{\epsilon} \tag{8}$$

with $c_\mu = 0.09$ (Launder et al., 1984).

Boundary conditions are specified to close the hydrodynamic formulation. A free-slip condition is applied at the lateral closed boundaries, allowing tangential flow while enforcing zero normal velocity. A no-slip condition is imposed at a distance from the sediment bed that depends on the surface roughness, defined as $z_0 = \frac{k_s}{30}$, where k_s is the equivalent Nikuradse roughness length, which is presently modelled as proportional to the mean grain size of the inlet sediment mixture. A logarithmic law of the wall is assumed in the near-bed region, consistent with the defined roughness lengths. This allows the bottom boundary conditions to be expressed as:

$$\frac{\nu_V}{h}\frac{\partial u}{\partial \sigma}\bigg|_{\sigma=-1} = \frac{\tau_b}{\rho} \qquad \text{and} \qquad w|_{\sigma=-1} = 0 \,, \tag{9}$$

where τ_b is the bed shear stress, which depends on the magnitude of the horizontal velocity in the first layer above the bed and on the bottom

roughness. At the free surface ($\sigma = 0$), dynamic and kinematic boundary conditions are imposed as:

$$\frac{\nu_V}{h}\frac{\partial u}{\partial \sigma}\bigg|_{\sigma=0} = 0 \qquad \text{and} \qquad w|_{\sigma=0} = 0\,. \tag{10}$$

The free surface elevation itself is computed separately via the continuity equation and is not assumed to be constant.

Finally, Dirichlet-type boundary conditions are prescribed for the turbulence closure variables k and ϵ as given by:

$$k\big|_{\sigma=0} = 0, \qquad \epsilon\big|_{\sigma=0} = 0\,, \tag{11}$$

$$k\big|_{\sigma=-1} = \frac{u_*^2}{\sqrt{c_\mu}}, \qquad \epsilon\big|_{\sigma=-1} = \frac{u_*^3}{\kappa\, z_1}\,. \tag{12}$$

where u_* is the friction velocity corresponding to the total bed shear stress, $\kappa = 0.4$ the von Kármán constant, z_1 the distance from the bed to the centre of the first computational layer, and $c_\mu = 0.09$.

2.2. Sediment transport

The suspended sediment concentration for each sediment class, $c^{(n)}$, is computed by solving the following advection–diffusion equation:

$$\frac{\partial c^{(n)}}{\partial t} + \frac{\partial (u c^{(n)})}{\partial x} + \frac{\partial [(w - w_s^{(n)}) c^{(n)}]}{\partial z} = \frac{\partial}{\partial x}\left(\epsilon_{s,x}\frac{\partial c^{(n)}}{\partial x}\right) + \frac{\partial}{\partial z}\left(\epsilon_{s,z}\frac{\partial c^{(n)}}{\partial z}\right) + S\,, \tag{13}$$

where $w_s^{(n)}$ is the hindered settling velocity of sediment class n, $\epsilon_{s,x}$ and $\epsilon_{s,z}$ are the sediment eddy diffusivity coefficients in the horizontal and vertical directions, respectively. These coefficients are assumed to be equal to the corresponding horizontal and vertical eddy viscosity values and are therefore independent of sediment grain size. The term S represents external sources or sinks of sediment concentration.

In sediment-laden flows, the settling velocity of sediment particles can be significantly reduced due to interparticle friction caused by the presence of other suspended sediments. This phenomenon, known as hindered settling, is modelled as a function of the non-hindered settling velocity $w_{s,0}^{(n)}$ and the local total sediment concentration according to Richardson and Zaki (1954)

$$w_s^{(n)} = \left(1 - \frac{c^{tot}}{C_{ref}}\right)^5 w_{s,0}^{(n)}\,, \tag{14}$$

where C_{ref} is a reference concentration and c^{tot} is the total mass concentration of suspended sediments, obtained by summing the concentrations of all sediment classes. The non-hindered settling velocity $w_{s,0}^{(n)}$ is computed using the expression proposed by Dietrich (1982), which improves upon Stokes' law (Stokes, 1851) by incorporating a drag coefficient that varies with the grain Reynolds number:

$$w_{s,0}^{(n)} = \frac{(s^{(n)} - 1) g d_s^{(n)2}}{18\,\nu_w}\,, \tag{15}$$

where $s^{(n)}$ is the specific gravity of sediment class n, defined as the ratio of sediment density $\rho_s^{(n)}$ to water density ρ_w, $d_s^{(n)}$ is the characteristic grain diameter, and ν_w is the kinematic viscosity of water.

At the free surface, the vertical diffusive flux of sediment is set to zero:

$$\frac{\partial c^{(n)}}{\partial z}\bigg|_{z=\zeta} = -\frac{w_s^{(n)} c^{(n)}}{\epsilon_{s,z}}\bigg|_{z=\zeta}\,, \tag{16}$$

while at the bed, it is governed by the balance between entrainment and deposition:

$$\frac{\partial c^{(n)}}{\partial z}\bigg|_{z=z_b} = -\frac{(-D^{(n)} + E^{(n)} - w_s^{(n)} c^{(n)})}{\epsilon_{s,z}}\bigg|_{z=z_b} \tag{17}$$

where $D^{(n)}$ and $E^{(n)}$ are the deposition and erosion rates of sediment class n, respectively. The deposition rate is given by:

$$D^{(n)} = w_s^{(n)} c_b^{(n)}\,, \tag{18}$$

and the erosion rate by:

$$E^{(n)} = \epsilon_{s,z}\frac{\partial c^{(n)}}{\partial z}\,. \tag{19}$$

In these expressions, c_b is the near-bed concentration, evaluated assuming the Rouse vertical distribution:

$$c_b^{(n)} = c_a^{(n)}\left[\frac{a(h - z_b)}{z_b(h - a)}\right]^{Z^{(n)}}\,, \tag{20}$$

where $Z^{(n)}$ is the Rouse number of the sediment class n defined by:

$$Z^{(n)} = \frac{w_s^{(n)}}{\kappa u_*}, \tag{21}$$

with κ the von Kármán constant, u_* the friction velocity corresponding to the total bed shear stress, a the reference distance from the bed (taken as 0.01 h), and $c_a^{(n)}$ the reference concentration at height a. Following van Rijn (1993), the reference concentration is computed as

$$c_a^{(n)} = 0.015\rho_s^{(n)}\frac{d_s^{(n)} T^{(n)1.5}}{a D_*^{(n)0.3}}\,, \tag{22}$$

where $D_*^{(n)}$ and $T^{(n)}$ are respectively the dimensionless grain size and bed shear stress given by

$$D_*^{(n)} = d_s^{(n)}\left[\frac{(\rho_s^{(n)}/\rho_w - 1) g}{\nu_w^2}\right]^{1/3}\,, \quad T^{(n)} = \frac{\tau_b - \tau_c^{(n)}}{\tau_c^{(n)}}\,,$$

where τ_b is the bed shear stress, and $\tau_c^{(n)}$ is the critical shear stress for sediment class n, based on a parametrization of the classical Shields curve.

Finally, the suspended load of sediment class n is calculated as

$$q_s^{(n)} = \int_{z_b + a}^{\zeta}\left(u c^{(n)} - \epsilon_{s,z}\frac{\partial c^{(n)}}{\partial x}\right) dz\,. \tag{23}$$

where the integration is performed from the reference elevation above the bed to the free surface ζ. Below the reference level a, sediment transport is assumed to be dominated by bedload, which is calculated following the formulation of van Rijn (1993):

$$q_b^{(n)} = 0.006\rho_s^{(n)} w_s^{(n)} d_s^{(n)}\sqrt{M^{(n)}}\, M_e^{(n)0.7}\,, \tag{24}$$

where M^n is sediment mobility number and M_e^n is excess sediment mobility number for sediment fraction (n).

2.3. Bed composition and evolution

Bed elevation is updated at each computational time step based on the net mass exchange between the flow and the bed for each sediment class. These exchanges are converted into elevation changes using class-specific dry bulk densities, which account for sediment porosity. The evolving bed topography and composition are then used to inform the hydrodynamic and sediment transport calculations, enabling a fully dynamic coupling between flow and morphodynamics.

A key feature of this study is the advanced representation of bed composition, modelled through a set of N sediment mass fractions, $\mathcal{F}^{(n)}$, corresponding to each sediment class n. These fractions vary in time and space, subject to the constraint $\sum_{n=1}^{N}\mathcal{F}^{(n)} = 1$. Bed composition is then implemented using two alternative approaches: a uniformly well-mixed bed and a stratified, layer-resolving formulation. A schematic illustration of these two approaches and their respective approximations for representing a sediment bed composed of a series of turbidite deposits is shown in Fig. 1.

The well-mixed bed approach treats the sediment layer as a single, homogeneous unit in which all sediment classes are fully mixed according to their evolving proportions. These fractions are considered equally available for entrainment at any time. The initial bed composition is defined by specifying sediment fractions either as uniform

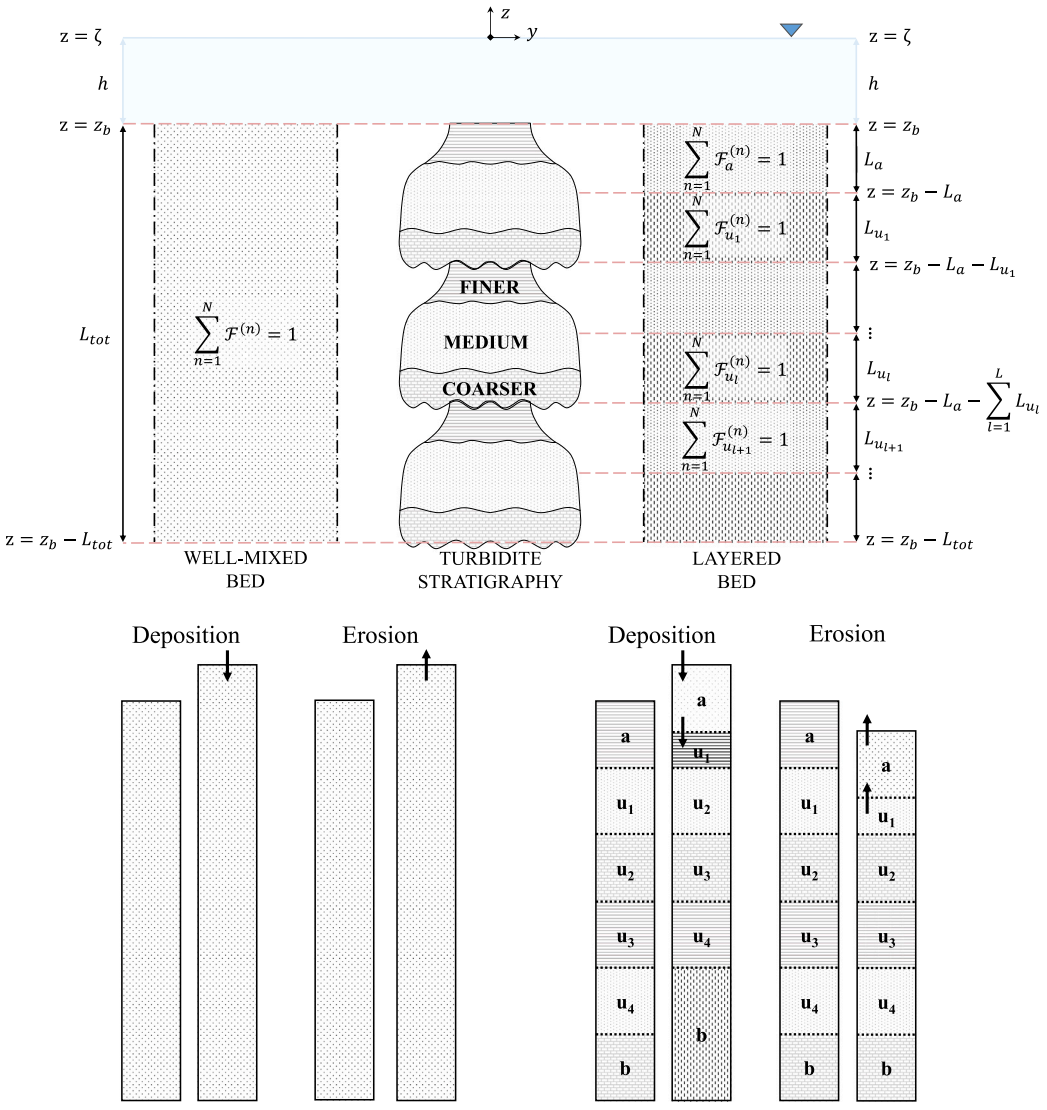

Fig. 1. Schematic side view of the water column above a sediment bed composed of a superposed series of three turbidites (center), with finer sediments at the top, medium sediments in the middle, and coarser sediments at the bottom. The thick solid line indicates the free surface elevation ($z = \zeta$), while thin lines delineate sediment layer boundaries. On the left and right are the corresponding approximations used in the modelling: a well-mixed bed (left), where sediment composition is uniform throughout, and a layered bed (right), where vertical heterogeneity is represented through discrete layers. Each layer l is characterized by a set of sediment mass fractions $\mathcal{F}_{(l)}^{(n)}$, one for each sediment class n. Layer thicknesses are denoted by L, with subscripts a, u, and tot referring to the active layer, underlayers, and total sediment bed thickness, respectively.

values or spatially varying fields in horizontal directions. The layer thickness is then computed from the total mass and the user-defined dry bulk densities for each sediment class, presently assumed constant among the considered classes. The bed surface corresponds to the top of this mixed layer. Being computationally efficient compared to more complex bed models, this approach has been widely used in morphodynamic modelling. However, it lacks the ability to capture vertical heterogeneity and track the depositional history, and thus cannot represent the internal structure of turbidite deposits. Its main limitation lies in the assumption that all sediment fractions are equally available for entrainment, which prevents the model from reproducing the selective erosion of specific grain sizes positioned at the flow-bed interface. This limitation is particularly relevant when studying erosive turbidity currents, which progressively expose and interact with the stratified layers of the bed.

Alternatively, sediment exchange between the bed and the water column is modelled using an extended version of the classical active layer approach (Hirano, 1971). In this formulation, the bed consists of two well-mixed layers: a surface active layer of constant thickness L_a (Church and Haschenburger, 2017), which interacts dynamically with the flow, and an underlying, inactive substrate layer. In this study, we adopt a more advanced multi-layer formulation in which the layered approach is also applied to the passive substrate (Deltares, 2025). The selection of this model is motivated by the need to explicitly resolve the vertical stratigraphy of the deposit, which is hypothesized to be a key control on self-acceleration. This approach discretizes the bed into distinct layers, overcoming the limitations of the well-mixed assumption, enabling the reproduction of the interaction between the flow and a vertically heterogeneous bed, such as the erosion of fine-grained caps typical of turbidites. This allows the definition of distinct bookkeeping layers beneath the active layer that represent the vertical

heterogeneity in bed composition, enabling explicit tracking of depositional history. The substrate is divided into L well-mixed underlayers, each with a thickness $L_{u^{(l)}}$ and a maximum allowed thickness $L_{u^{(l)},\max}$, along with an underlying base layer that is not subject to thickness constraints. These underlayers primarily serve as storage or buffer zones and can be assigned different sediment compositions. The thickness of the base layer, L_b, is computed as the total bed thickness L_{tot} minus the combined thickness of the active layer and underlayers.

In the well-mixed bed approach, changes in sediment composition only occur within a single active layer of defined thickness ($L_a = L_{tot}$). Erosion and deposition instantaneously alter the composition of the entire layer. Conversely, in the layered bed approach, these instantaneous processes only affect the topmost layers. During deposition, sediment settled from the water column to the bed is added to the active layer and mixed with its existing content, affecting only the topmost erodible bed layer instantaneously. If the active layer exceeds its defined thickness, the excess is transferred to the topmost underlayer. Once an underlayer reaches its maximum thickness, a new underlayer is created, provided the maximum number of underlayers $U_{\max}$ has not been reached. If this limit is exceeded, the lowest underlayer is merged with the base layer at the bottom of the bed. Conversely, during erosion, sediment is first removed from the active layer. To maintain its specified thickness, it is replenished with material from the topmost underlayer. If this underlayer is exhausted, the process continues with the next layer below.

The layered bed approach provides a more accurate representation of evolving bed composition. When flow conditions entrain finer but not coarser particles, erosion selectively removes fine sediment from the active layer. As this layer is replenished from the underlayer below, its new composition reflects that of the top underlayer. This sorting effect is however confined to the upper layers, while deeper layers remain unaffected, allowing the model to preserve inner bed composition over time.

Finally, morphodynamic evolution is computed using the sediment continuity equation, also known as the Exner equation, which in the present 2DV framework simplifies to the following one-dimensional form:

$$\frac{\partial z_b}{\partial t} = -\frac{1}{1-\lambda_p}\sum_{n=1}^{N}\frac{\partial q^{(n)}}{\partial x}\,, \tag{25}$$

where z_b is the bed elevation (positive upward), λ_p is the bed porosity, and $q^{(n)}$ is the depth-integrated sediment transport rate per unit width for sediment class n, which includes both bed-load $q_b^{(n)}$ and suspended-load $q_s^{(n)}$.

2.4. Model setup

Table 1 presents a summary of the key model parameters adopted. The computational domain extends 15 m in length with a constant 5% slope, consistent with their flume setup (Fig. 2). A structured grid with uniform horizontal spacing of 0.05 m was used, and 92 sigma layers were applied in the vertical to capture flow and density gradients. Vertical resolution was refined near the bed to better resolve sediment transport processes and their influence on density gradients, with the lowest layer thickness set to 0.1% of the local water depth. The simulation time step was 0.015 s.

A spin-up period of a few minutes was applied, during which no inlet sediment concentration was introduced and bed elevation was held constant. During this phase, the upstream open boundary, corresponding to an inlet water depth H_0 of 50 cm, was forced with a steady inflow velocity U_0 of 60 cm/s, consistent with the inlet conditions of Experiment 6 from Sequeiros et al. (2018). A Riemann boundary condition was imposed at the downstream boundary to permit outgoing waves to exit the domain without reflection (Verboom and Slob, 1984).

After the spin-up interval, sediment was introduced at the upstream boundary. A sediment particle density ρ_s of 1530 kg/m^3 was used to mimic the plastic sediment employed in the experiments. To assess sediment sorting effects, the inflow consisted of a mixture of three grain-size classes ($N = 3$): fine ($d_f = 40$ μm, $F_f = 0.25$), medium ($d_m = 60$ μm, $F_m = 0.5$), and coarse ($d_c = 80$ μm, $F_c = 0.25$), with grain sizes and mass fractions based on the probability density function reported by Sequeiros et al. (2018). This discretization of the continuous grain-size distribution represents a balance between computational efficiency and physical realism, designed to capture the essential features of sediment sorting while maintaining tractable computational requirements. Following their laboratory setup, inflow velocity and sediment concentrations were prescribed to match the reported inlet discharge. Specifically, the inlet section was forced with a total sediment concentration $C_0^{(n)}$ of 31 kg/m^3. These conditions were applied near the free surface, where the water–sediment mixture was introduced via a diffuser.

Table 1
Summary of key parameters used in the numerical model setup.

Description	Symbol	Value	Unit
Domain length	L_x	15	m
Background bottom slope	s	0.05	–
Longitudinal spacing	Δx	0.05	m
σ-layer number	N_σ	92	–
σ-layer bottom thickness	$\Delta\sigma_b$	0.0005	m
Hydrodynamic time-step	Δt	0.015	s
Spin-up interval	Δt_{up}	300	s
Inlet water depth	H_0	0.5	m
Inlet flow velocity	U_0	0.6	m/s
Sediment density	ρ_s	1530	kg/m^3
Sediment class number	N	3	–
Sediment mean grain sizes	$d_s^{(n)}$	40, 60, 80	μm
Inlet sediment concentration	$C_0^{(n)}$	31	kg/m^3
Roughness length	k_s	0.001	m
Sediment porosity	λ_p	0.4	–
Reference concentration	C_{ref}	918	kg/m^3
Active layer thickness	L_a	0.001	m
Underlayer number	L	3	–
Maximum underlayer thickness	$L_{n,max}$	0.002	m

All model runs were performed with a mobile (erodible) bed, except for an initial simulation in which the bed was treated as non-erodible to represent the flume bottom. This initial run served as a base case to generate the first deposit. Subsequent turbidity currents were simulated over this deposit. A spatially uniform bottom roughness was applied, defined by an equivalent roughness length k_s proportional to the mean grain size of the inlet sediment. Net sediment mass exchanges between the flow and bed were converted into bed elevation changes using a porosity $\lambda_p = 0.4$, corresponding to a dry bed density of 918 kg/m^3, comparable to the reference concentration C_{ref} used in the hindered settling formulation. These values were assumed constant across all simulations and bed conditions because the laboratory experiments utilized granular plastic sediment. Unlike natural sediments, this material does not undergo significant compaction with depth, justifying the use of fixed porosity and dry density values regardless of the deposit thickness or stratigraphy.

For the simulation using the layered bed approach, the active layer thickness L_a was set to a uniform value of 1 mm, consistent with the stratigraphic layer thicknesses observed in the experimental turbidites. This value represents the relevant vertical scale of flow-bed interaction and aligns with the millimetre-scale exchange layer prescribed in other turbidity current models (Naruse and Nakao, 2021; Cai and Naruse, 2021). Three underlayers were defined beneath the active layer, each with a maximum thickness equal to 2 mm, over an initial rigid base layer.

Regarding numerical verification, tests with varying spatial and temporal resolutions were conducted. The model showed no signs of ill-posed behaviour, such as grid-dependent spurious oscillations or active-layer-thickness-dependent instability (Stecca et al., 2014; Chavarrías

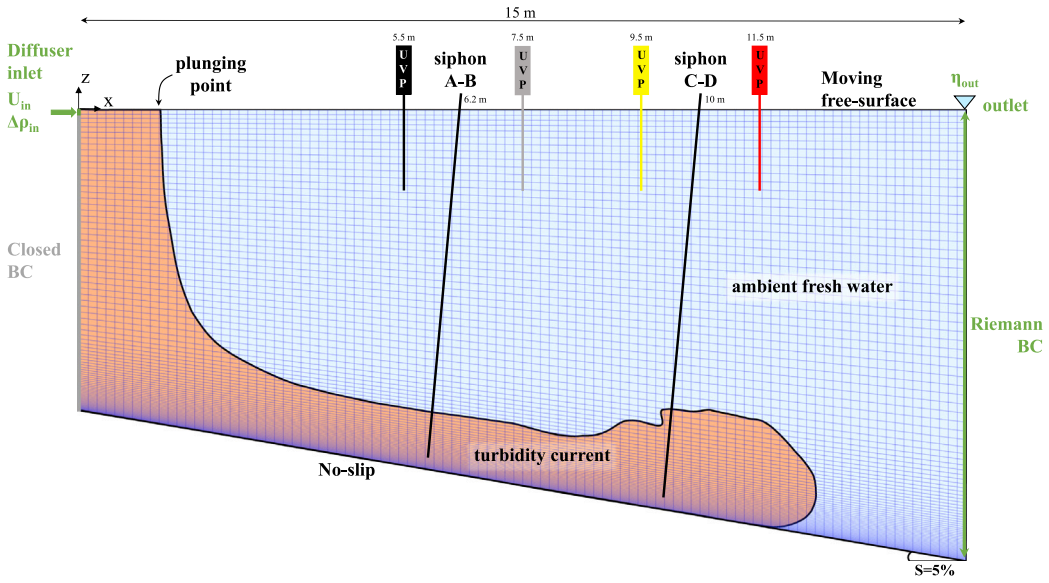

Fig. 2. Schematic of the experimental flume setup by Sequeiros et al. (2018) and the corresponding numerical model domain.

Table 2
Summary of the numerical experiment series. The setup for each case (Runs 1–3) is derived from the depositional output of the Base Case (Run 0), with the details of the bottom boundary used in each simulation.

Run #	Initial deposit	Initial slope	Primary focus	Bed sediment	Bed composition
0	None	5%	Base Deposit	None	Rigid bottom
1	5 × Base Deposit	5.3%	Steeper slope	Unimodal	Five superposed deposits
2	Base Deposit	5%	Downstream fining	Poorly sorted	Well-mixed deposit
3	Base Deposit	5%	Vertical layering	Poorly sorted	Layered deposit

et al., 2018), and sensitivity analysis confirmed that results are robust to variations in active layer thickness as well as horizontal viscosity and diffusivity parameters (see Appendix for details).

3. Results

This section presents a series of numerical simulations aimed at replicating and elucidating the self-acceleration phenomenon observed in the laboratory experiments of Sequeiros et al. (2018). Each run was performed with identical inlet flow and sediment discharges, corresponding to experimental conditions of Experiment 6 from their study, which produced continuous downslope self-acceleration.

The only input parameters varied across the simulations were those related to the modelled bed elevation and composition, which were systematically changed to investigate the influence of different depositional features on flow dynamics.

The bed configurations summarized in Table 2 were designed to systematically isolate and evaluate the individual contributions of specific depositional features to the self-acceleration process. Run 0 provides the baseline deposit and demonstrates that an erodible bed is a necessary condition for self-acceleration. Run 1 tests the isolated effect of increased bed slope with a simplified unimodal sediment, removing the complexity of grain-size sorting to assess how bathymetric conditioning alone influences flow dynamics. Run 2 introduces longitudinal grain-size variability using the well-mixed bed formulation, allowing assessment of downstream fining effects without vertical stratification. Run 3 incorporates the full complexity of a vertically stratified bed, representing the natural fining-upward structure of turbidite deposits. This structured approach incrementally increases the complexity of the sediment bed to isolate and identify the bed characteristics required to sustain self-accelerating flow regimes.

3.1. Modelled turbidite deposit (Run 0)

The initial simulation (Run 0) served as a base case to evaluate the model's ability to reproduce key depositional processes. It simulated a single turbidity current propagating over a rigid, non-erodible bed, thereby generating a sediment deposit directly comparable to the experimental results of Sequeiros et al. (2018). The primary aim was to assess whether the model could capture the fundamental features of turbidite deposition.

The resulting bed composition agrees well with the experimental measurements, displaying clear longitudinal grain-size sorting. A progressive downstream fining is evident, with coarser particles deposited proximally and finer particles transported farther downslope. Fig. 3 shows the along-slope profiles of the bed elevation for each sediment class, as well as the total deposit thickness. The spatial distribution of the sediment fractions reproduces the sorting trends reported by Sequeiros et al. (2018), including the variations in d_{16} and d_{84} grain sizes along the flume (see right panel of Fig. 3). Fine sediment is spread uniformly, while coarser material accumulates upstream, consistent with the experimental observations. Moreover, the model effectively replicates key depositional features, generating a sediment highpoint near the plunging point (at approximately 1.5 m from the inlet), followed by a gradual downstream thinning of the deposit, consistent with the laboratory experiment's results.

The model also reproduces deposit thickness with good accuracy: at 4 m from the inlet, a deposit thickness of approximately 7 mm matches the value measured at the same location for Experiment 5 (see Figure 12 in Sequeiros et al., 2018). This agreement, together with the accurate reproduction of downstream fining, demonstrates the model's capability to simulate realistic turbidite deposition. The resulting bed thickness and composition, formed under controlled non-erodible conditions, were then used to setup the bottom boundary

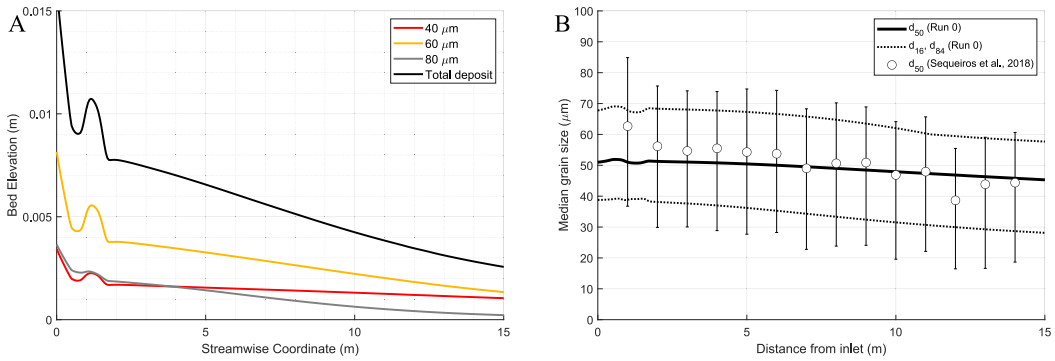

Fig. 3. (A) Modelled sediment deposit at the end of Run 0. Final bed elevation (black line) is shown along the streamwise coordinate, along with the contribution of individual sediment fractions (d_f = 40 μm - red line, d_m = 60 μm - yellow line, d_c = 80 μm - grey line). (B) Grain size distribution along the channel comparing numerical results with experimental data. The solid black line indicates the median grain size (d_{50}) from the numerical simulation (Run 0), with the dotted lines representing the 16th (d_{16}) and 84th (d_{84}) percentiles. The white circles show the experimental median grain size (d_{50}) from the bed after the last turbidity current in the experiments. The corresponding vertical bars denote the range between the experimental d_{16} and d_{84}.

conditions for the subsequent simulations involving erodible beds of increasing complexity.

In this base-case scenario, the turbidity current displayed a decelerating regime in the upper flume, maintaining nearly constant peak velocities, followed by downstream deceleration. Fig. 7 compares the simulated velocities at four cross-sections along the flume (locations shown in Fig. 2) with those recorded during Experiment 6: the first observed self-accelerating current in their experimental series. While the measurements reveal a current that continuously accelerates downslope, the Run 0 modelled flow (Fig. 7, black dotted line) clearly decelerates due to sediment deposition, lacking the bed entrainment necessary to sustain momentum. The simulation indicates a strong correlation between near-bed sediment concentration and flow velocity. The near-bed concentration peaks at around to 6 kg/m^3 at a distance of 7.5 m from the inlet (Fig. 7C). This location coincides with the maximum modelled velocity. Downstream from this point, the flow gradually decelerates, decreasing by more than 1 cm/s over a distance of 4 m, and both concentration and velocity reach a minimum near the 11.5 m section (Fig. 7G). This confirms that, under the prescribed inflow conditions, the flow is dissipative in the absence of dynamic interaction with an erodible bed.

3.2. Steeper erodible bed (Run 1)

Run 1 was designed to test whether a steeper bed slope, resulting from the cumulative aggradation of successive turbidite deposits, could trigger alone the self-acceleration process. The initial bed topography for Run 1 was setup by superposing five identical deposits, each representing the sediment deposited during Run 0, to simulate the cumulative deposition induced by five consecutive turbidity currents. The resulting bottom featured an average slope of approximately 5.3%, slightly steeper than the original 5 % flume slope. The bed elevation profile is shown in Fig. 4, where each grey line represents the bed surface following one flow event. The thick black line corresponds to the final bed profile that was used as initial bottom boundary for Run 1. The trend of this reconstructed profile fits well with the final profile of the experiments, showing a peak in deposition in the plunging zone and a downstream thinning of the bed. The erodible bed was assumed to be composed of a unimodal sediment with a grain size of 60 μm. This value was selected to represent the median grain size ($d_{50} \approx 57$ μm) of the lightweight plastic sediment employed in the reference laboratory experiments. Using this representative diameter allows the model to capture the primary entrainment processes observed experimentally, without accounting for secondary effects such as sediment sorting in longitudinal and vertical directions.

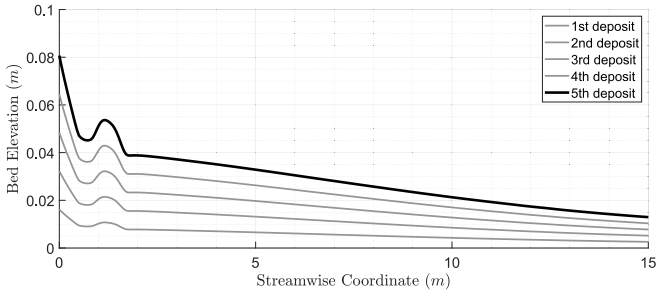

Fig. 4. Modelled bottom boundary at the beginning of Run 1. Grey lines represent the thickness of the deposit of Run 0, while the thick black line is the initial bed elevation profile used in Run 1 as built upon the cumulative deposition induced by a series of five consecutive turbidity currents.

The combination of the increased slope and the availability of a unimodal erodible sediment bed resulted in a self-accelerating/bypassing regime. An initial flow velocity of approximately 10 cm/s was observed in the proximal section (Fig. 7A, blue dash line), accompanied by an increase in near-bed sediment concentrations (Fig. 7B). This was followed by sustained acceleration in the medial sections, where velocities increased to 13 cm/s and subsequently to 13.5 cm/s (Fig. 7C and 7E), while near-bed concentrations reached 6.5 kg/m^3 (Fig. 7D and 7F). Further downstream, peak flow velocities stabilized at approximately 13.5 cm/s (Fig. 7G), and near-bed sediment concentrations began to decline slightly (Fig. 7H).

These subtle yet measurable differences in flow velocity and density down the flume indicate that slope steepening due to cumulative deposition can facilitate the onset of self-acceleration, even when the increase in slope is relatively minor compared to the background gradient. However, the current was only ignited in the upstream sections, where the local slope increase was more pronounced, suggesting that slope enhancement alone is insufficient to sustain self-acceleration throughout the entire flume length.

3.3. Downstream fining (Run 2)

Run 2 was designed to investigate the influence of downstream fining on turbidity current dynamics. The initial bed was constructed using the deposit produced by Run 0, preserving the longitudinal grain-size variation obtained by that simulation by accounting for a poorly sorted sediment bed composed of the three different fractions. Sediments were implemented using the well-mixed bed approach, meaning that while the relative proportions of fine, medium, and coarse fractions

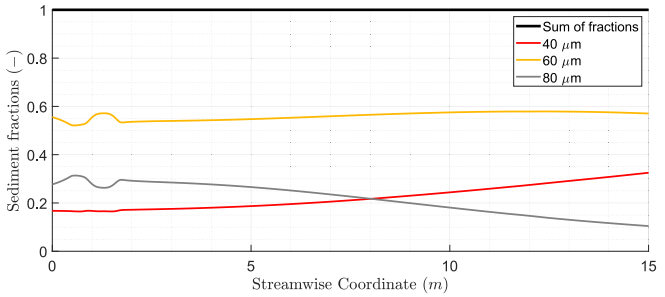

Fig. 5. Initial distribution of modelled sediment fractions within the well-mixed bed for Run 2. The streamwise profiles of each grain-size class are shown: fine (d_f = 40 μm, red), medium (d_m = 60 μm, yellow), and coarse (d_c = 80 μm, grey). The black line indicates the sum of all sediment fractions, which remains equal to one along the entire flume length, confirming mass conservation in the initial bed configuration.

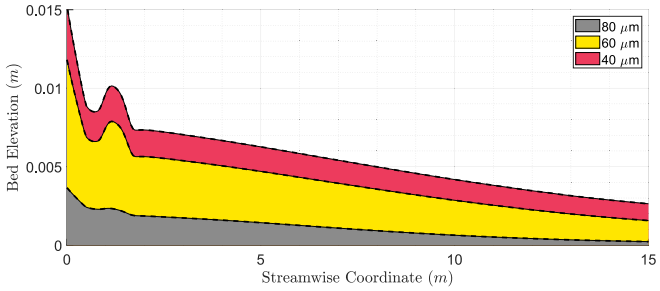

Fig. 6. Initial vertically stratified sediment deposit used in Run 3. The bed consists of three distinct sediment layers arranged along the streamwise coordinate: a fine-grained surface layer (d_f = 40 μm, red), underlain by a medium-grained layer (d_m = 60 μm, yellow), and a coarse-grained basal layer (d_c = 80 μm, grey). The dashed black lines delineate the interfaces between sediment layers and the top surface of the total deposit.

varied along the flume, each vertical column of bed material remained compositionally uniform. This setup allowed downstream fining to be represented without vertical stratification. Fig. 5 shows the initial spatial distribution of sediment fractions in Run 2: the proportion of the finest fraction increases from approximately 17 % near the inlet to over 30 % downstream, while the coarsest fractions decline accordingly. Notably, the intermediate 60 μm fraction remains remarkably constant, constituting about 50 % of the sediment along the entire streamwise direction. The downstream fining observed here is consistent with the findings of Sequeiros et al. (2018), who also documented a systematic reduction in grain size with increasing distance from the inlet.

Simulation results for Run 2 (Fig. 7, green dotted line) closely resemble those of Run 1, showing a self-accelerating/bypassing regime. However, flow velocities exhibit a slight increase not only in the proximal section but also in the distal sections, where the bed became increasingly enriched in finer sediment and the current reached a maximum velocity of 14 cm/s (Fig. 7G). In contrast to Run 1, both peak velocities and excess densities showed a slight increase between the two downstream monitoring stations. This trend was accompanied by a net erosional regime, with the model predicting a gradual rise in excess density along the flume, a result of sustained sediment entrainment from the bed. These findings suggest that downstream fining enhances the potential for self-acceleration sustenance downslope by increasing fine sediment availability and erodibility, thereby promoting more efficient sediment uptake by the flow.

3.4. Vertical stratification (Run 3)

Run 3 was designed to investigate how the vertical stratification of the sediment bed impacts the turbidity current dynamics, and particularly its self-acceleration. As in Run 2, the initial bed consisted of a poorly sorted sediment mixture, with a longitudinal grain-size distribution matching that of the final deposit from Run 0. However, in this simulation, a layered-bed approach was implemented to represent a vertically structured bed with coarsening downward, mimicking natural turbidite stratigraphy.

The bed was configured to resemble a complete Bouma-like sequence, characterized by finer sediment at the surface and progressively coarser material with depth. In this setup, the fine fraction formed the uppermost active layer in direct contact with the flow, underlain by the first underlayer composed of the medium fraction, with the coarse fraction forming the basal layer of the stratified deposit. Fig. 6 illustrates this vertically stratified initial bed configuration. This setup of the bottom boundary conditions allowed the isolation of the effects of vertical stratification on the onset and development of self-acceleration.

Simulation results from Run 3 (Fig. 7, red continuous line) revealed the development of a turbidity current that self-accelerates, characterized by a sustained increase in flow velocity and concentration along the flume. Maximum horizontal velocities increase from approximately 11 cm/s in the 5.5 m section (Fig. 7A) to 13.5 cm/s in the intermediate sections (Fig. 7C and E), ultimately reaching a maximum of around 14.5 cm/s in the downstream section (Fig. 7G). Similar trends are also evident in the concentrations, which reach a maximum (7 kg/m^3) in the downstream cross-section where the velocity is greater (Fig. 7H). This acceleration was driven by the enhanced entrainment of fine-grained sediment from the active layer, which formed the uppermost part of the vertically stratified bed. Because the most erodible material was immediately accessible at the flow–bed interface throughout the model domain, continuous entrainment occurred. This, in turn, progressively increased the flow's excess density, enhancing its downslope gravitational driving force and sustaining acceleration.

4. Discussion

The results of our numerical experiments demonstrate that turbidity currents achieve self-acceleration only when the sediment bed is represented with sufficient geological realism. In particular, the inclusion of downslope fining and vertical stratification, morphological features commonly observed in both laboratory and natural turbidite systems, emerges as a prerequisite for properly reproducing self-accelerating flows.

The following subsections discuss in detail the individual contributions of bed composition, bed slope, and flow discharge to the onset and sustenance of self-acceleration, along with the underlying physical mechanisms controlling these processes.

4.1. Effects of bed composition

Simulations with simplified bed configurations, such as the non-erodible bed in Run 0, produced flows that were primarily dissipative in the distal flume and attained only neutral buoyancy in medial sections, with no clear signs of self-acceleration.

To assess the effects of including only a unimodal erodible bed, we conducted an additional simulation (Run 1) with the same input parameters as Run 0, but imposing a homogeneous layer of 60 μm sediment along the entire length of the flume. This simulation produces a purely bypassing flow, revealing that the presence of a homogeneous sediment bed is not a sufficient condition for both the onset and sustenance of self-acceleration.

A marked shift in flow behaviour occurred when more realistic bed heterogeneity was introduced. In Run 2, where the bed exhibited downstream fining, the flow began to self-accelerate all the way down

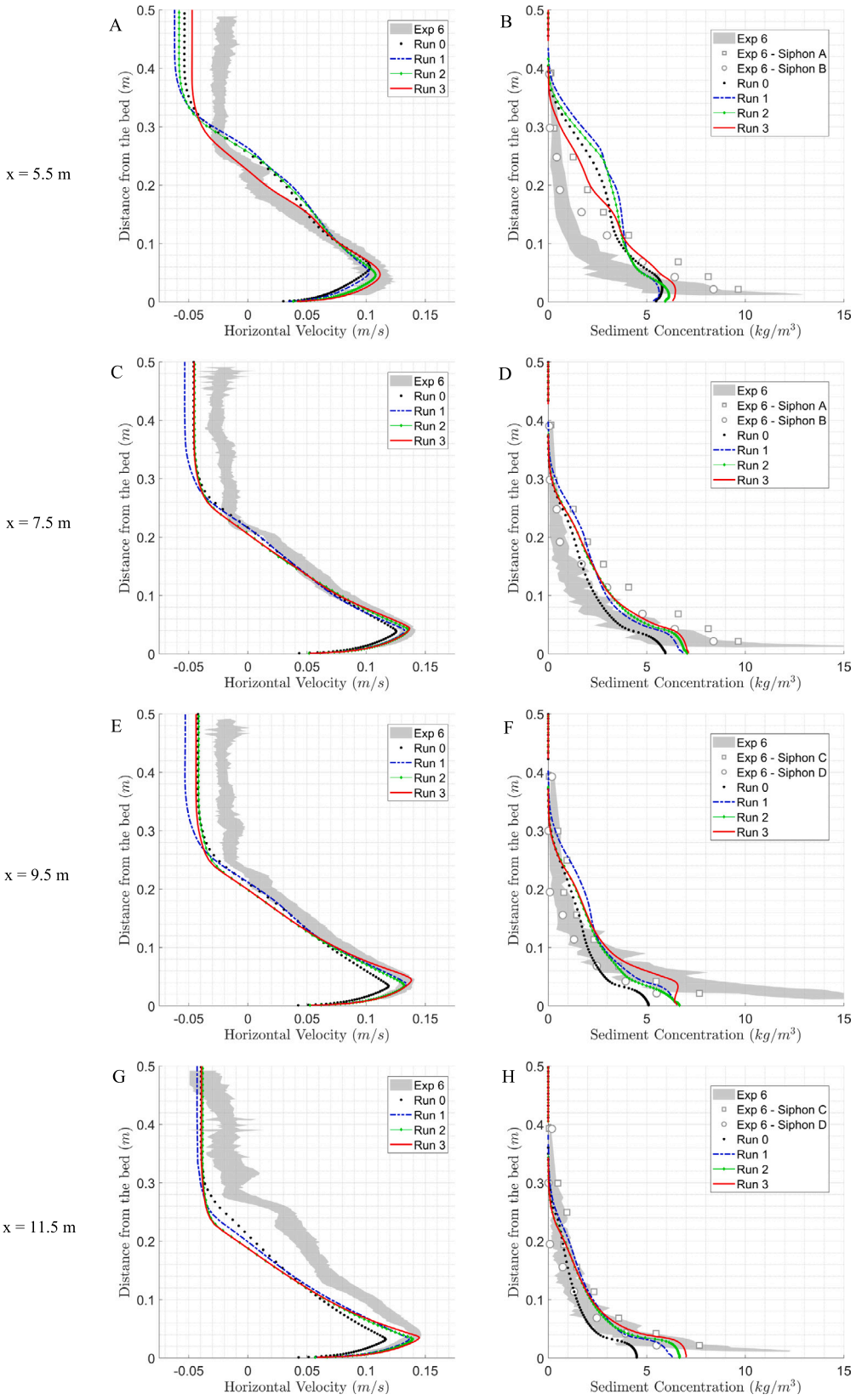

Fig. 7. Comparison of simulated and experimental vertical profiles of horizontal velocity and sediment concentration at varying distances from the inlet. The left column (A, C, E, G) illustrates horizontal velocity (m/s) while the right column (B, D, F, H) depicts sediment concentration (kg/m^3). Experimental data are shown as grey shaded areas. Distances from the inlet are indicated by the panel grouping: (A–B) 5.5 m, (C–D) 7.5 m, (E–F) 9.5 m, and (G–H) 11.5 m. Simulated data is shown for the four different runs: Run 0 (black dotted line), Run 1 (blue dashed line), Run 2 (green dotted line), and Run 3 (red continuous line).

the flume length. This effect was further amplified in Run 3, which included vertical stratification with the finer erodible material overlaying coarser sediment. These more realistic bed configurations enabled the sustained downstream entrainment of fine particles, increasing the flow's excess density and thus providing the additional gravitational forcing required for self-acceleration. The results of numerical Run 3 showed the best match to spatial variations in velocity and density of the self-accelerating flow Experiment 6 of Sequeiros et al. (2018). Our results underscore the critical role of bed sediment heterogeneity, both longitudinal and vertical, in controlling turbidity current dynamics.

The physical mechanisms through which bed composition controls self-acceleration can be understood by examining the interactions between sediment entrainment, flow stratification, and turbulence production. In Run 3, the fine-grained surface layer is characterized by a lower critical shear stress for erosion compared to the coarser fractions beneath. As the turbidity current entrains this easily erodible material, the near-bed sediment concentration increases, directly enhancing the flow's excess density according to (5). This density increase amplifies the horizontal pressure gradient (4), which represents the primary driving force for turbidity currents on sloping beds.

Furthermore, the entrainment of fine sediment affects the vertical structure of the flow through two competing mechanisms. On one hand, the addition of suspended sediment increases the buoyancy production term B in the turbulent kinetic energy Eq. (6), which tends to dampen turbulence and hinder vertical mixing. On the other hand, the flow acceleration induced by the enhanced excess density increases the velocity shear near the bed, thereby augmenting the turbulence production term P. In the self-accelerating flows of Run 3, the latter mechanism prevails: the increased bed shear stress τ_b associated with higher near-bed velocities sustains sufficient turbulent mixing to maintain sediment in suspension while simultaneously enhancing sediment entrainment from the active layer. This positive feedback loop, whereby erosion increases density, which increases velocity, which increases bed shear stress and further erosion, constitutes the fundamental mechanism of self-acceleration first theorized by Parker et al. (1986).

The role of grain size in this feedback is critical. Fine sediments are characterized by lower settling velocities (15) and correspondingly lower Rouse numbers (21), enabling them to remain suspended throughout the flow depth rather than concentrating near the bed. This vertical distribution of fine sediment is more efficient at maintaining the flow's excess density and driving force relative to coarser material, which tends to settle rapidly and contribute less to flow momentum. The downstream fining in Run 2 and the fine-grained surface layer in Run 3 thus provide a continuous source of sediment that can be efficiently incorporated into suspension, sustaining the self-acceleration process over the entire flume length.

The specific arrangement of particle sizes within the bed exerts a fundamental control on the flow's potential for self-acceleration. As observed in Run 3, the presence of a fine-grained active layer facilitates the preferential entrainment of sediment with low settling velocities. Interpreted through the theoretical framework of Stacey and Bowen (1988), such fine sediment is expected to be distributed throughout the water column, providing the gravitational driving force required to maintain the flow. While a layer-averaged approach integrates properties over the flow depth, the efficient acceleration in Run 3 is consistent with the physical principle that fines (characterized by low Rouse numbers) contribute to excess density over a greater flow thickness, whereas coarser grains tend to remain confined near the bed (Bolla Pittaluga et al., 2018). This theoretical vertical partitioning — where fines drive the flow bulk while coarser fractions interact with the boundary — provides a robust physical explanation for why beds with available fines (either through downstream fining or vertical stratification) are more effective at triggering ignition. Conversely, when the bed is composed of coarser material (Run 1), the higher settling velocity promotes rapid deposition, theoretically limiting the sediment load to the near-bed region and hindering the development of the large-scale density contrast needed to sustain acceleration downstream.

4.2. Effects of bed slope

The physical basis for the slope effect lies in its influence on the gravitational driving force acting on the turbidity current. An increase in bed slope directly enhances the downslope component of gravity acting on the excess density of the flow.

A unimodal erodible bed in combination with an increased slope due to cumulative deposition (Run 1) promotes self-acceleration in the proximal flume. We find that even subtle changes in bed slope, of an order of magnitude lower than the background bed gradient, can significantly affect the onset of self-acceleration, but this effect is insufficient to promote its sustenance all the way down the flume length.

To further investigate the importance of the enhanced slope, we conducted an additional simulation examining the individual effects of bed slope, without accounting for any sediment bed availability. This simulation did not produce any flow acceleration downslope, demonstrating that the slope increase alone results in a local increase in flow acceleration but it is not sufficient to sustain continued acceleration downstream.

These results imply that even modest variations in seabed slope can influence the self-acceleration potential of turbidity currents, provided the bed is erodible. However, slope increase by itself is not sufficient because sustaining the feedback requires an adequate — and correctly represented — distribution of erodible sediment at the bed (i.e., spatially and vertically varying composition/availability, not a uniform surface).

4.3. Effects of flow discharge

In this study, we focus mainly on the importance of turbidite depositional processes, but also the effect of an enhanced inlet discharge warrants further discussion, particularly dealing with plunging self-accelerating flows like those presently investigated. Based on the series of experiments documented in Sequeiros et al. (2018), flow discharge likely plays a role in achieving self-acceleration. They indeed crossed the threshold conditions for self-acceleration by gradually increasing the inlet flow discharge, documenting experiments with relatively low inlet discharges that developed into depositional and decelerating currents.

We performed a final additional simulation with a unimodal erodible bed and a flow discharge of 2 L/s, significantly larger than the 1.8 L/s used in our previous numerical tests and generally larger than all the experiments of Sequeiros et al. (2018), whose higher flow discharge equals 1.88 L/s. This simulation resulted in the most downstream plunging point location. Sediment deposition and erosion upstream and at the plunging point were similar to those previously modelled, but with slightly higher turbidity current velocities and densities just downstream of it. Such increased energy corresponded to a larger erosion of the 60 μm sediment all along the flume and the highest flow velocity modelled at the most downstream measuring section, which equals 15 cm/s.

The physical mechanism underlying the discharge effect may be related to the increased sediment mass flux delivered to the turbidity current. Given that the inlet sediment concentration remains constant across simulations, a higher discharge directly increases the total sediment mass entering the system per unit time. Although the plunging zone represents a region of flow reorganization where the horizontal velocity approaches zero at the plunging point and part of the inlet momentum may be dissipated, the increased sediment supply is transferred to the turbidity current downstream of it. This results in a higher excess density of the current, which enhances the gravitational

driving force acting on the flow. The resulting acceleration increases the bed shear stress τ_b, promoting sediment entrainment from the bed and potentially triggering the positive feedback loop required for self-acceleration. However, the relative contributions of inlet momentum transfer and sediment mass flux in controlling the downstream flow dynamics remain unclear, and further investigations focusing on the hydrodynamics of the plunging mechanism are needed to clarify these effects.

These results show that higher flow rates can induce marked downslope flow accelerations, reinforcing the idea already mentioned by Sequeiros et al. (2018) that even simple hydrodynamic drivers are capable of triggering sustained self-acceleration. Further studies concerning the influence of increased flow and sediment discharges on the plunging mechanism are needed to better clarify how all these hydro-sedimentary factors interact.

4.4. Implications for numerical modelling and natural systems

The additional simulations demonstrate that the mere presence of erodible sediment at the bed is a necessary but not sufficient condition for turbidity current self-acceleration; additional hydro-sedimentary factors must also be accounted for to initiate and sustain the self-acceleration process. Specifically, critical factors include the inlet configuration, the inflow discharge, the inlet sediment concentration, the location of the plunging point, and the spatial/vertical distribution of erodible sediment along the bed.

State-of-the-art turbidity current models often treat the bed as uniformly erodible or even impose a predefined erosion–deposition balance (auto-suspension), without explicitly resolving the sedimentary structure of the bed. While such simplifications are useful for certain applications, they overlook the critical influence of bed composition, particularly the immediate availability of fine sediment at the flow–bed interface, on sediment entrainment and resulting flow evolution. Our results demonstrate that neglecting spatial variations in the sediment bed composition can lead to significant underestimation of turbidity current acceleration.

Although earlier theoretical and numerical studies, such as those by Fukushima et al. (1985) and Parker et al. (1986), recognized the importance of fine sediment availability for sustaining turbidity currents, they did not quantify how the grain-size distribution of the underlying deposit controls the turbidity current self-acceleration process. We fill that gap by demonstrating, in a laboratory-scale context, that the stratigraphy of experimental turbidites, shaped by preceding depositional events, provides the sediment "fuel" necessary for ignition and continued flow acceleration.

These findings suggest that the depositional history of sediment beds directly and actively influences the behaviour of turbidity current events. We identify three key sedimentary features as primary drivers of self-acceleration: (1) bathymetric conditioning, whereby an even mild increase in slope of the sedimented bed fosters the onset of self-acceleration, (2) longitudinal sorting, which causes the flow to encounter progressively finer, more erodible material downslope, and (3) vertical stratification, where fine, easily entrained sediment is positioned at the flow–bed interface. These features are natural and predictable outcomes of turbidity current deposition and are commonly observed in turbidite sequences.

This study demonstrates that these sedimentary structures are not merely passive geological records of past events, but instead play an active role in shaping the dynamics of subsequent flows. Their presence can significantly enhance the potential for self-acceleration by promoting sustained sediment entrainment and increasing flow density, with important implications for understanding and predicting turbidity current behaviour in natural settings. In particular, subaqueous systems characterized by recent, fine-grained deposits may be especially susceptible to hosting self-accelerating, erosive, and therefore potentially hazardous turbidity currents.

The extrapolation of the present numerical results to real-scale turbidity currents is supported by principles of dynamic similarity, in particular by the equivalence of the densimetric Froude number (Fr_d). As established by Sequeiros et al. (2009), although the Reynolds numbers of laboratory currents are orders of magnitude lower than those of field-scale flows, both regimes fall fully within the turbulent range, ensuring the applicability of the Reynolds-number independence principle. Caution is nevertheless required regarding hydraulic resistance. Laboratory flows often operate in hydraulically smooth regimes, whereas submarine canyons are characterized by hydraulically rough conditions. However, as noted by Sequeiros et al. (2018), this discrepancy implies that laboratory conditions are energetically conservative: relative frictional losses (normalized by flow volume) are larger in the laboratory due to wall effects and the lower Re. Therefore, the ignition and self-acceleration observed and modelled in this study represent a robust lower bound on the potential of natural flows; in a real canyon, where the ratio between gravitational driving forces and frictional resistance is more favourable, the self-acceleration mechanism is likely even more efficient. Comparison with field data further supports this validity. Normalized vertical velocity profiles obtained in analogous experimental configurations show an excellent collapse with profiles measured in the Monterey Submarine Canyon (Xu et al., 2004), confirming that the internal turbulent structure scales geometrically. In addition, the numerical reproduction of erosion-driven flow sustenance is consistent with recent observations in the Congo Canyon (Azpiroz-Zabala et al., 2017), confirming the critical role of bed sediment entrainment in prolonging the flow run-out over long distances.

The corollary of our study is that the history of sedimentation near the source of turbidity currents, e.g. at the heads of submarine canyons, may impact the frequency of future events, particularly those that can reach high velocities and are capable of impacting submarine infrastructure. Thus, the occurrence of large, potentially destructive turbidity currents must depend not only on large triggering events such as large storms, but also on the availability of fine sediment deposited from previous depositional events.

5. Conclusions

A series of numerical simulations was designed to investigate the conditions under which turbidity currents self-accelerate. We reproduced laboratory-scale turbidity currents under varying bottom boundary conditions, enabling a systematic evaluation of modelled depositional processes and the controls they exert on flow behaviour.

The main conclusions of this study are:

- The numerical model, which was previously validated only against hydrodynamic measurements, is able to also replicate depositional processes typical of turbidite deposits; namely their thickness thinning, sediment fining, and vertical stratification.
- Geological realism in the representation of bed elevation and sediment composition is essential for triggering and developing turbidity current self-acceleration. Self-acceleration was only observed when the sediment bed included the aforementioned realistic depositional features of turbidite systems.
- Simplified bed conditions inhibit self-acceleration. Simulations over a non-erodible bed (Run 0) and over a unimodal, uniformly erodible bed (without adding further slope) resulted in flows that were non-accelerating.
- Even subtle changes in bed slope, an order of magnitude lower than the background gradient, can induce the onset of self-acceleration (Run 1), however this effect alone is insufficient to promote its sustenance all the way down the flume length.
- Downstream fining also promotes flow acceleration. When the bed was modelled with longitudinal grain-size sorting (Run 2), the flow self-accelerates along the entire flume due to increased entrainment of fine sediment down the slope.

- Vertical stratification further enhances self-acceleration. Incorporating a layered bed structure with a fine-grained surface layer (Run 3), the self-acceleration process was amplified by providing a continuous source of sediment from the easily erodible material at the flow–bed interface.
- Bed heterogeneity is a key control on turbidity current behaviour. The spatial distribution of sediment grain sizes, both longitudinally and vertically, not only reflects depositional history, but actively governs the potential for subsequent flows to self-accelerate.
- Underwater environments underlain by recently deposited, fine-grained erodible sediments may be particularly susceptible to the formation of self-accelerating and erosive turbidity currents, with increased potential for submarine hazards such as cable or pipeline damage.

These findings have direct practical implications for hydraulic engineering and the risk assessment of subsea infrastructure. Current engineering practices often rely on numerical models that treat the seabed as a homogeneous boundary; our results demonstrate that such simplifications can lead to significant underestimation of flow velocities and run-out distances. Consequently, effective hazard mitigation for submarine cables and pipelines requires site surveys that go beyond bathymetry to include detailed geotechnical characterization of bed stratigraphy and grain-size trends.

Future research should aim to extend this analysis to three-dimensional domains to investigate how bed heterogeneity interacts with complex canyon topographies, such as channel bends and constrictions. Additionally, further work is needed to explore the influence of the plunging mechanism and higher flow discharges on sediment entrainment, as well as the potential role of cohesive forces and bed consolidation in modulating the erodibility of stratified deposits.

CRediT authorship contribution statement

Umberto Sasso: Analysis and interpretation of data, Writing – original draft. **Gaetano Porcile:** Conception and design of study, Supervision, Writing – review & editing. **Octavio E. Sequeiros:** Data curation, Writing – review & editing. **Carlos Pirmez:** Conception and design of study, Writing – review & editing. **Michele Bolla Pittaluga:** Conception and design of study, Supervision, Writing – review & editing.

Declaration of competing interest

The authors declare that they have no known competing financial interests or personal relationships that could have appeared to influence the work reported in this paper.

Acknowledgements

Umberto Sasso acknowledges financial support provided through an industrial PhD fellowship at the Department of Civil, Chemical and Environmental Engineering (DICCA), University of Genoa. The fellowship is funded under the Regional Programme European Social Fund Plus (ESF+/FSE+) 2021–2027 (Priority 2 – Education and Training; Specific Objective ESO 4.6 / OS-f), with industrial co-funding from the University spin-off company Weather Water Sand. Additional financial support for supervision activities by Dr. Gaetano Porcile (co-supervisor and member of the PhD committee) was provided directly by the spin-off company.

Appendix. Model verification

Grid convergence was assessed using the Run 0 configuration (depositional flow over a rigid bed) by comparing simulations with horizontal resolutions of Δx = 0.1 m, 0.05 m, and 0.025 m, with time steps halved accordingly. Fig. A.1 shows vertical profiles of horizontal velocity and sediment concentration at x = 5.5 m and x = 11.5 m for Run 0 conditions. As summarized in Table A.1, the results at the upstream location (x = 5.5 m) are largely grid-independent, with variations relative to the selected grid remaining below 0.7% for peak horizontal velocity and 1.3% for peak concentration. Conversely, at the downstream location (x = 11.5 m), the solution exhibits higher sensitivity to spatial resolution, with deviations on the finest mesh reaching approximately 7.9% for velocity and 15.6% for concentration. Consequently, the Δx = 0.05 m resolution was adopted as a balanced compromise between computational efficiency and accuracy.

Table A.1
Mesh independence verification for Run 0: peak horizontal velocity (v) and peak sediment concentration (c) at locations x = 5.5 m and x = 11.5 m. Values in parentheses represent the relative percentage difference with respect to the chosen baseline resolution (Δx = 0.05 m).

Case	Δt [s]	x-s [m]	Peak v [m/s]	Peak c [kg/m^3]
Δx = 0.1 m	0.03	5.5	0.1026 (−0.48%)	5.7579 (−0.29%)
Δx = 0.05 m	**0.015**	**5.5**	**0.1031**	**5.7749**
Δx = 0.025 m	0.0075	5.5	0.1038 (+0.68%)	5.7016 (−1.29%)
Δx = 0.1 m	0.03	11.5	0.1111 (−4.64%)	4.2045 (−6.38%)
Δx = 0.05 m	**0.015**	**11.5**	**0.1165**	**4.4912**
Δx = 0.025 m	0.0075	11.5	0.1073 (−7.89%)	3.789 (−15.64%)

Table A.2
Sensitivity to active-layer thickness using Run 3 configuration: peak horizontal velocity and peak density at x = 5.5 m and x = 11.5 m. Percent changes are relative to the baseline case (L_a = 1 mm).

Case	x-s [m]	Peak v [m/s]	Peak c [kg/m^3]
L_a = 0.1 mm	5.5	0.1118 (+0.009%)	6.457 (+0.043%)
L_a = 0.5 mm	5.5	0.11178 (−0.009%)	6.4537 (−0.008%)
L_a = 1 mm	**5.5**	**0.11179**	**6.4542**
L_a = 1.5 mm	5.5	0.11181 (+0.018%)	6.6541 (−0.03%)
L_a = 0.1 mm	11.5	0.14524 (+0.339%)	7.06022 (+0.9%)
L_a = 0.5 mm	11.5	0.14514 (+0.269%)	7.03172 (+0.493%)
L_a = 1 mm	**11.5**	**0.14475**	**6.9972**
L_a = 1.5 mm	11.5	0.14465 (−0.069%)	6.9971 (−0.001%)

Sensitivity to active layer thickness was evaluated using the Run 3 configuration (stratified erodible bed) over the range 0.1–1.5 mm (Fig. A.2). As shown in Table A.2, the model exhibits minimal sensitivity to this parameter at both upstream (x = 5.5 m) and downstream (x = 11.5 m) locations. Deviations from the baseline case (L_a = 1 mm) are negligible, remaining consistently below 0.4% for peak horizontal velocity and 0.9% for peak concentration across the entire domain. These results demonstrate that the model solution is robust relative to the choice of L_a within physically reasonable bounds.

The influence of horizontal diffusivity was examined for the self-accelerating Run 3 by varying the Schmidt number (Sc). The Schmidt number is a dimensionless parameter defined as the ratio of momentum diffusivity to mass diffusivity. In the context of sediment-laden flows, it relates the turbulent eddy viscosity ν_H to the horizontal eddy diffusivity ϵ_x according to $Sc = \nu_H/\epsilon_x$. A Schmidt number equal to unity implies that momentum and suspended sediment are diffused at the same rate by turbulent eddies, while values less than unity indicate that sediment is dispersed more efficiently than momentum. The choice of Schmidt number affects the horizontal spreading of suspended sediment concentration gradients, which in turn can influence the longitudinal evolution of the turbidity current.

The Schmidt number was varied from 1 to 0.25 (Fig. A.3), including a zero background diffusivity case. As detailed in Table A.3, the model sensitivity to this parameter is primarily reflected in the scalar field distribution. Decreasing Sc (i.e., enhancing horizontal mixing) leads to a systematic reduction in peak concentration, due to the lateral

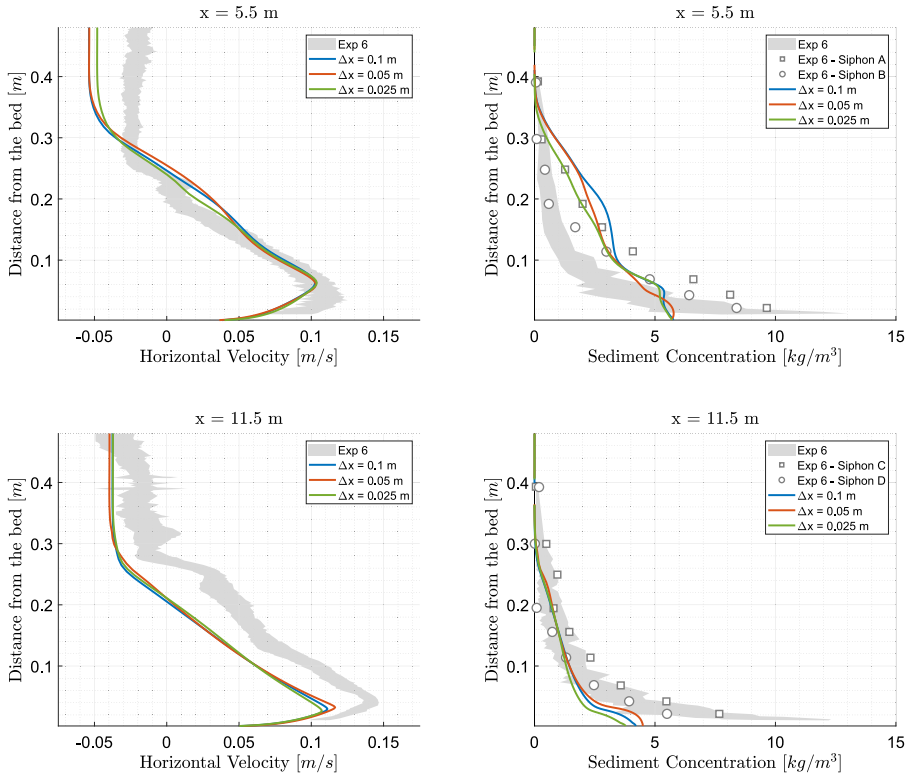

Fig. A.1. Mesh independence verification for Run 0. Vertical profiles of horizontal velocity (left column) and sediment concentration (right column) are compared at two streamwise locations: x = 5.5 m (top row) and x = 11.5 m (bottom row). The comparison includes three longitudinal grid spacings (Δx = 0.1 m in blue, 0.05 m in orange, and 0.025 m in green) against the experimental data (Exp. 6) in grey.

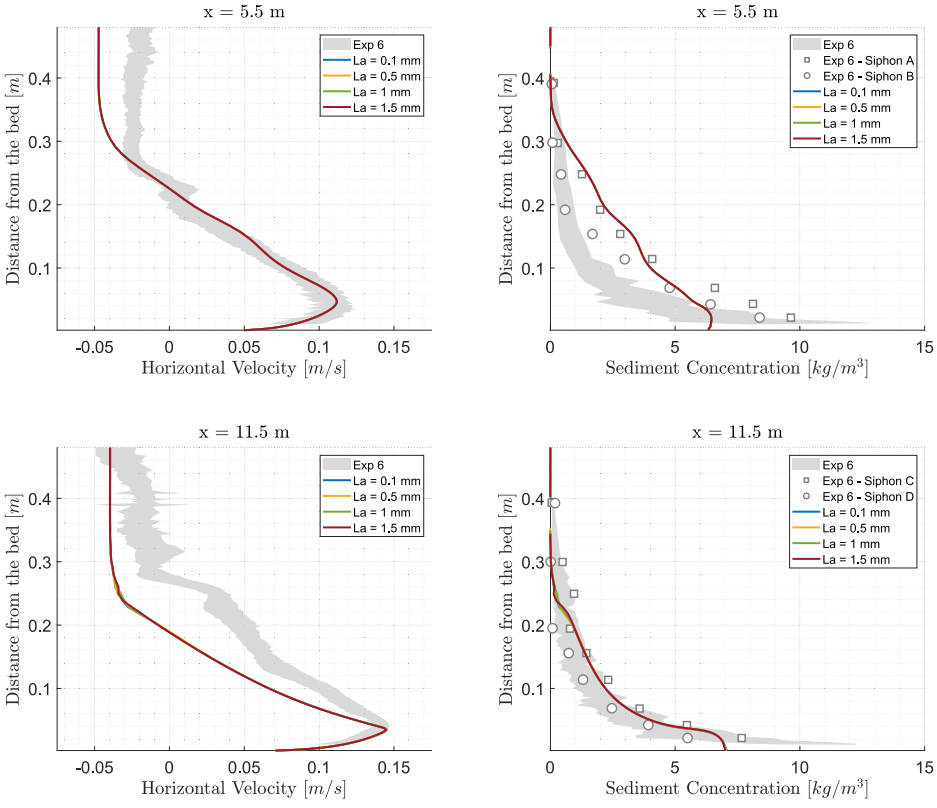

Fig. A.2. Sensitivity analysis to active-layer thickness for Run 3. Vertical profiles of horizontal velocity (left column) and sediment concentration (right column) are compared at two streamwise locations: x = 5.5 m (top row) and x = 11.5 m (bottom row). The comparison includes four active-layer thickness values (L_a = 0.1 mm in blue, 0.5 mm in yellow, 1 mm in green, and 1.5 mm in red) against the experimental data (Exp. 6) in grey.

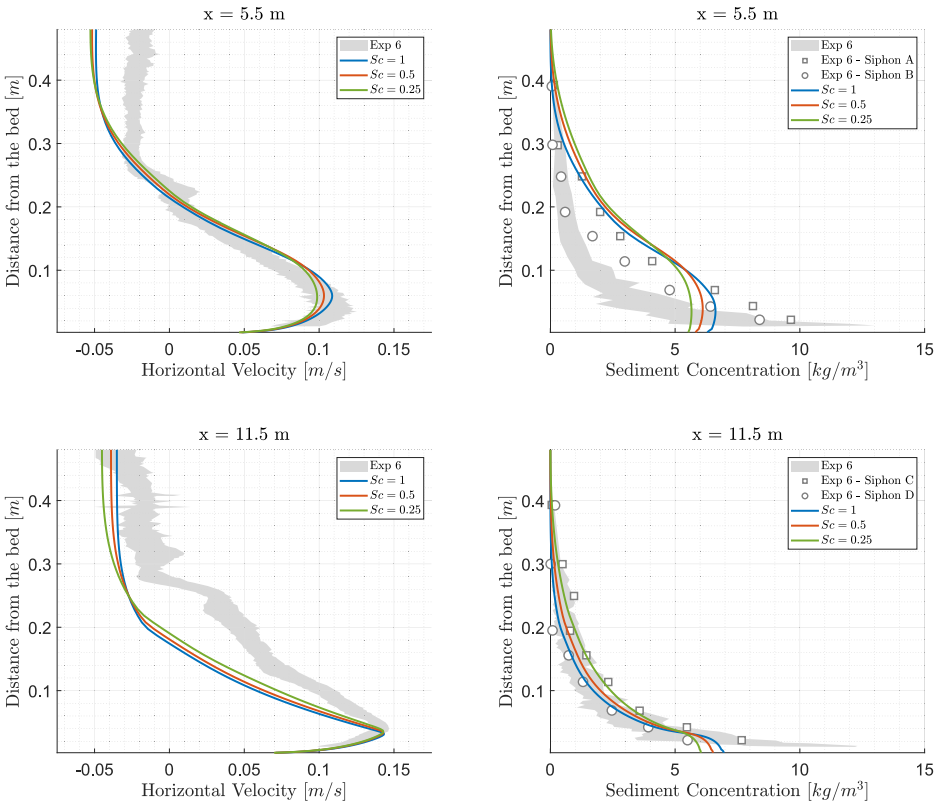

Fig. A.3. Sensitivity analysis to Schmidt number for Run 3. Vertical profiles of horizontal velocity (left column) and sediment concentration (right column) are compared at two streamwise locations: $x = 5.5$ m (top row) and $x = 11.5$ m (bottom row). The comparison includes three Schmidt number values ($Sc = 1$ in blue, 0.5 in orange, and 0.25 in green) against the experimental data (Exp. 6) in grey.

Table A.3
Sensitivity to Schmidt number (Sc) using Run 3 configuration: peak horizontal velocity (v) and peak sediment concentration (c) at locations $x = 5.5$ m and $x = 11.5$ m. Values in parentheses represent the relative percentage difference with respect to the baseline case ($Sc = 1$).

Case	x-s [m]	Peak v [m/s]	Peak c [kg/m^3]
$Sc = 1$	**5.5**	**0.1087**	**6.619**
$Sc = 0.5$	5.5	0.1033 (−4.97%)	6.107 (−7.74%)
$Sc = 0.25$	5.5	0.099 (−8.92%)	5.658 (−14.52%)
$Sc = 1$	**11.5**	**0.1433**	**6.951**
$Sc = 0.5$	11.5	0.1428 (−0.35%)	6.516 (−6.26%)
$Sc = 0.25$	11.5	0.1428 (−0.35%)	6.033 (−13.21%)

spreading of the sediment cloud, with drops of approximately 14.5% at $x = 5.5$ m and 13.2% at $x = 11.5$ m for the lowest Schmidt number tested ($Sc = 0.25$). Despite this reduction in peak density values, the flow dynamics remain remarkably consistent. At the downstream location ($x = 11.5$ m), the peak horizontal velocity shows negligible variations ($< 0.4\%$) across all cases. This indicates that while the horizontal diffusivity parameter affects the spatial distribution of the suspended load (lowering the peak values), it does not disrupt the global positive feedback loop between erosion and acceleration. The overall gravitational driving force sustained by the active entrainment of sediment remains sufficient to drive the flow, demonstrating that the self-acceleration mechanism is robust to the choice of the horizontal diffusivity parameter.

References

Azpiroz-Zabala, M., Cartigny, M.J.B., Talling, P.J., Parsons, D.R., Sumner, E.J., Clare, M.A., Simmons, S.M., Cooper, C., Pope, E.L., 2017. Newly recognized turbidity current structure can explain prolonged flushing of submarine canyons. Sci. Adv. 3, e1700200. http://dx.doi.org/10.1126/sciadv.1700200.

Baker, M.L., Hage, S., Talling, P.J., Acikalin, S., Hilton, R.G., Haghipour, N., Ruffell, S.C., Pope, E.L., Jacinto, R.S., Clare, M.A., Sahin, S., 2024. Globally significant mass of terrestrial organic carbon efficiently transported by canyon-flushing turbidity currents. Geology 52, 631–636. http://dx.doi.org/10.1130/G51976.1.

Bolla Pittaluga, M., Frascati, A., Falivene, O., 2018. A gradually varied approach to model turbidity currents in submarine channels. J. Geophys. Res.: Earth Surf. 123, 80–96. http://dx.doi.org/10.1002/2017JF004331.

Bouma, A.H., 1962. Sedimentology of Some Flysch Deposits: A Graphic Approach to Facies Interpretation. Elsevier, Amsterdam.

Cai, Z., Naruse, H., 2021. Inverse analysis of experimental scale turbidity currents using deep learning neural networks. J. Geophys. Res.: Earth Surf. 126, http://dx.doi.org/10.1029/2021JF006276, 2021JF006276.

Carter, L., Burnett, D., Drew, S., Marle, G., Hagadorn, L., Bartlett-McNeil, D., Irvine, N., 2009. Submarine Cables and the Oceans: Connecting the World. UNEP-WCMC Biodiversity Series No. 31. ICPC/UNEP/UNEP-WCMC, Cambridge, UK, http://dx.doi.org/10.34892/FC3W-X186.

Carter, L., Gavey, R., Talling, P.J., Liu, J.T., 2014. Insights into submarine geohazards from breaks in subsea telecommunication cables. Oceanography 27, 58–67. http://dx.doi.org/10.5670/oceanog.2014.40.

Chavarrías, V., Stecca, G., Blom, A., 2018. Ill-posedness in modeling mixed sediment river morphodynamics. Adv. Water Resour. 114, 219–235. http://dx.doi.org/10.1016/j.advwatres.2018.02.011.

Choi, S.U., García, M.H., 2002. k-ϵ turbulence modeling of density currents developing two dimensionally on a slope. J. Hydraul. Eng. 128, 55–63. http://dx.doi.org/10.1061/(ASCE)0733-9429(2002)128:1(55).

Church, M., Haschenburger, J.K., 2017. What is the "active layer"? Water Resour. Res. 53, 5–10. http://dx.doi.org/10.1002/2016WR019675.

Cooper, C.K., Wood, J., Imran, J., Islam, A., Wright, P., Faria, R., Tati, A., Casey, Z., Casey, R.T., 2016. Designing for turbidity currents in the Congo Canyon. In: Offshore Technology Conference. Offshore Technology Conference, http://dx.doi.org/10.4043/26919-MS, OTC–26919–MS.

Deltares, 2025. Delft3D-Flow User Manual. Delft, The Netherlands, Version 4.05 - 80213.

Dietrich, W.E., 1982. Settling velocity of natural particles. Water Resour. Res. 18, 1615–1626. http://dx.doi.org/10.1029/WR018i006p01615.

Eggenhuisen, J.T., Tilston, M.C., de Leeuw, J., Pohl, F., Cartigny, M.J.B., 2020. Turbulent diffusion modelling of sediment in turbidity currents: An experimental

validation of the Rouse approach. Depos. Rec. 6, 203–216. http://dx.doi.org/10.1002/dep2.86.

Fazel Mojtahedi, F., Yousefpour, N., Chow, S.H., Cassidy, M., 2025. Offshore turbidity currents forecasting (part i): Integrating deep learning and computational fluid dynamics. Ocean Eng. 331, 121360. http://dx.doi.org/10.1016/j.oceaneng.2025.121360.

Frascati, A., Bolla Pittaluga, M., Sequeiros, O.E., Pirmez, C., Cantelli, A., 2025. A channel centerline-based method for modeling turbidity currents morphodynamics: Case study of the Baco–Malaylay submarine canyon system. J. Mar. Sci. Eng. 13, 1495. http://dx.doi.org/10.3390/jmse13081495.

Fukushima, Y., Parker, G.D., Pantin, H.M., 1985. Prediction of ignitive turbidity currents in Scripps Submarine Canyon. Mar. Geol. 67, 55–81. http://dx.doi.org/10.1016/0025-3227(85)90148-3.

Garcia, M.H., 1994. Depositional turbidity currents laden with poorly sorted sediment. J. Hydraul. Eng. 120, 1240–1263. http://dx.doi.org/10.1061/(ASCE)0733-9429(1994)120:11(1240).

Garfield, N., Rago, T.A., Collins, C.A., Rischmiller, F.W., 1994. Evidence of a turbidity current in Monterey Submarine Canyon associated with the 1989 Loma Prieta earthquake. Cont. Shelf Res. 14, 673–686. http://dx.doi.org/10.1016/0278-4343(94)90112-0.

Gavey, R., Carter, L., Liu, J.T., Talling, P.J., Hsu, R., Pope, E., Evans, G., 2017. Frequent sediment density flows during 2006 to 2015, triggered by competing seismic and weather events: Observations from subsea cable breaks off southern Taiwan. Mar. Geol. 384, 147–158. http://dx.doi.org/10.1016/j.margeo.2016.06.001.

Gladstone, C., Phillips, J.C., Sparks, R.S.J., 1998. Experiments on bidisperse, constant-volume gravity currents: propagation and sediment deposition. Sedimentology 45, 833–843. http://dx.doi.org/10.1046/j.1365-3091.1998.00189.x.

Heerema, C.J., Talling, P.J., Cartigny, M.J.B., Paull, C.K., Bailey, L., Simmons, S.M., et al., 2020. What determines the downstream evolution of turbidity currents? Earth Planet. Sci. Lett. 532, 116023. http://dx.doi.org/10.1016/j.epsl.2019.116023.

Heezen, B.C., Ewing, M., 1952. Turbidity currents and submarine slumps, and the 1929 Grand Banks earthquake. Am. J. Sci. 250, 849–873. http://dx.doi.org/10.2475/ajs.250.12.849.

Hirano, M., 1971. River bed degradation with armoring. Proc. Jpn. Soc. Civ. Eng. 1971, 55–65. http://dx.doi.org/10.2208/jscej1969.1971.195_55.

Huang, H., Imran, J., Pirmez, C., 2005. Numerical model of turbidity currents with a deforming bottom boundary. J. Hydraul. Eng. 131, 283–293. http://dx.doi.org/10.1061/(ASCE)0733-9429(2005)131:4(283).

Huang, H., Imran, J., Pirmez, C., 2007. Numerical modeling of poorly sorted depositional turbidity currents. J. Geophys. Res.: Ocean. 112, C01014. http://dx.doi.org/10.1029/2006JC003778.

Hughes Clarke, J.E., 2016. First wide-angle view of channelized turbidity currents links migrating cyclic steps to flow characteristics. Nat. Commun. 7, 11896. http://dx.doi.org/10.1038/ncomms11896.

Inman, D.L., Nordstrom, C.E., Flick, R.E., 1976. Currents in submarine canyons: An air-sea-land interaction. Annu. Rev. Fluid Mech. 8, 275–310. http://dx.doi.org/10.1146/annurev.fl.08.010176.001423.

Kuenen, P.H., Migliorini, C.I., 1950. Turbidity currents as a cause of graded bedding. J. Geol. 58, 91–127. http://dx.doi.org/10.1086/625710.

Launder, B.E., Reynolds, W.C., Rodi, W., 1984. Turbulence Models and their Applications. Eyrolles, Paris.

Liu, J.T., Wang, Y.H., Yang, R.J., Hsu, R.T., Kao, S.J., Lin, H.L., Kuo, F.H., 2012. Cyclone-induced hyperpycnal turbidity currents in a submarine canyon. J. Geophys. Res.: Ocean. 117, C04033. http://dx.doi.org/10.1029/2011JC007630.

Lowe, D.R., 1982. Sediment gravity flows: Ii, depositional models with special reference to the deposits of high-density turbidity currents. J. Sediment. Res. 52, 279–297. http://dx.doi.org/10.1306/212F7F31-2B24-11D7-8648000102C1865D.

Lu, Y., Liu, X., Xie, X., Sun, J., Yang, Y., Guo, X., 2024a. Particle-scale analysis on dynamic response of turbidity currents to sediment concentration and bedforms. Phys. Fluids 36, 033316. http://dx.doi.org/10.1063/5.0191219.

Lu, Y., Liu, X., Yang, Y., Wang, D., Yu, H., Zhang, S., Xie, X., Guo, X., 2024b. Flow and depositional response of turbidity currents to complex canyon topographies: A numerical simulation perspective. Geomorphology 466, 109437. http://dx.doi.org/10.1016/j.geomorph.2024.109437.

Ma, H., Parker, G., Cartigny, M., Viparelli, E., Balachandar, S., Fu, X., Luchi, R., 2025. Two-layer formulation for long-runout turbidity currents: theory and bypass flow case. J. Fluid Mech. 1009, A19. http://dx.doi.org/10.1017/jfm.2025.246.

Mutti, E., 1985. Turbidite systems and their relations to depositional sequences. In: Zuffa, G. (Ed.), Provenance of Arenites. Springer Netherlands, pp. 65–93. http://dx.doi.org/10.1007/978-94-017-2809-6_4.

Naruse, H., Nakao, K., 2021. Inverse modeling of turbidity currents using an artificial neural network approach: verification for field application. Earth Surf. Dyn. 9, 1091–1109. http://dx.doi.org/10.5194/esurf-9-1091-2021.

Normandeau, A., Bourgault, D., Neumeier, U., Lajeunesse, P., St-Onge, G., Gostiaux, L., Chavanne, C., 2020. Storm-induced turbidity currents on a sediment-starved shelf: Insight from direct monitoring and repeat seabed mapping of upslope migrating bedforms. Sedimentology 67, 1045–1068. http://dx.doi.org/10.1111/sed.12673.

Normark, W.R., Piper, D.J.W., 1991. Initiation processes and flow evolution of turbidity currents: Implications for the depositional record. In: Osborne, R.H. (Ed.), In: From Shoreline to Abyss: Contributions in Marine Geology in Honor of Francis Parker Shepard, vol. 46, Society for Sedimentary Geology, pp. 207–230. http://dx.doi.org/10.2110/pec.91.09.0207.

Normark, W.R., Piper, D.J.W., Hiscott, R.N., 1989. Observed parameters for turbidity-current flow in channels, Reserve Fan, Lake Superior. J. Sediment. Res. 59, 423–431. http://dx.doi.org/10.1306/212F8FB2-2B24-11D7-8648000102C1865D.

Pantin, H.M., 1979. Interaction between velocity and effective density in turbidity flow: Phase-plane analysis, with criteria for autosuspension. Mar. Geol. 31, 59–99. http://dx.doi.org/10.1016/0025-3227(79)90057-4.

Parker, G., 1982. Conditions for the ignition of catastrophically erosive turbidity currents. Mar. Geol. 46, 307–327. http://dx.doi.org/10.1016/0025-3227(82)90086-X.

Parker, G., Fukushima, Y., Pantin, H.M., 1986. Self-accelerating turbidity currents. J. Fluid Mech. 171, 145–181. http://dx.doi.org/10.1017/S0022112086001404.

Parker, G., Fukushima, Y., Pantin, H.M., 1987. Experiments on turbidity currents over an erodible bed. J. Hydraul. Res. 25, 123–147. http://dx.doi.org/10.1080/00221688709499292.

Paull, C.K., Talling, P.J., Maier, K.L., Parsons, D., Xu, J., Caress, D.W., Gwiazda, R., Lundsten, E.M., Anderson, K., Barry, J.P., Chaffey, M., O'Reilly, T., Rosenberger, K.J., Gales, J.A., Kieft, B., McGann, M., Simmons, S.M., McCann, M., Sumner, E.J., Clare, M.A., Cartigny, M.J., 2018. Powerful turbidity currents driven by dense basal layers. Nat. Commun. 9, 4114. http://dx.doi.org/10.1038/s41467-018-06254-6.

Pope, E.L., Talling, P.J., Carter, L., 2017. Which earthquakes trigger damaging submarine mass movements: Insights from a global record of submarine cable breaks? Mar. Geol. 384, 131–146. http://dx.doi.org/10.1016/j.margeo.2016.01.009.

Porcile, G., Bolla Pittaluga, M., Frascati, A., Sequeiros, O.E., 2020. Typhoon-induced megarips as triggers of turbidity currents offshore tropical river deltas. Commun. Earth Environ. 1, 2.

Porcile, G., Bolla Pittaluga, M., Frascati, A., Sequeiros, O., 2023. Modelling the air-sea-land interactions responsible for the direct trigger of turbidity currents by tropical cyclones. Appl. Ocean Res. 137, 103602. http://dx.doi.org/10.1016/j.apor.2023.103602.

Porcile, G., Enrile, F., Besio, G., Bolla Pittaluga, M., 2022. Hydrostatic vs. non-hydrostatic modelling of density currents developing two dimensionally on steep and mild slopes. Appl. Ocean Res. 119, 103085. http://dx.doi.org/10.1016/j.apor.2022.103085.

Prior, D.B., Bornhold, B.D., Wiseman, W.J., Lowe, D.R., 1987. Turbidity current activity in a British Columbia fjord. Science 237, 1330–1333. http://dx.doi.org/10.1126/science.237.4820.1330.

Richardson, J.F., Zaki, W.N., 1954. Sedimentation and fluidization: Part i. Trans. Inst. Chem. Eng. 32, 35–53.

Salaheldin, T.M., Imran, J., Chaudhry, M.H., Reed, C., 2000. Role of fine-grained sediment in turbidity current flow dynamics and resulting deposits. Mar. Geol. 171, 21–38. http://dx.doi.org/10.1016/S0025-3227(00)00114-6.

Salinas, J., Balachandar, S., Shringarpure, M., Fedele, J., Hoyal, D., Cantero, M., 2020. Soft transition between subcritical and supercritical currents through intermittent cascading interfacial instabilities. Proc. Natl. Acad. Sci. USA 117, 18278–18284. http://dx.doi.org/10.1073/pnas.2008959117.

Sequeiros, O.E., Bolla Pittaluga, M., Frascati, A., Pirmez, C., Masson, D.G., Weaver, P., Crosby, A.R., Lazzaro, G., Botter, G., Rimmer, J.G., 2019. How typhoons trigger turbidity currents in submarine canyons. Sci. Rep. 9, 9220. http://dx.doi.org/10.1038/s41598-019-45615-z.

Sequeiros, O.E., Mosquera, R., Pedocchi, F., 2018. Internal structure of a self-accelerating turbidity current. J. Geophys. Res.: Ocean. 123, 6260–6276. http://dx.doi.org/10.1029/2018JC014061.

Sequeiros, O.E., Naruse, H., Endo, N., Garcia, M.H., Parker, G., 2009. Experimental study on self-accelerating turbidity currents. J. Geophys. Res.: Ocean. 114, C05025. http://dx.doi.org/10.1029/2008JC005149.

Sequeiros, O.E., Spinewine, B., Beaubouef, R.T., Sun, T., Garcia, M.H., Parker, G., 2010. Characteristics of velocity and excess density profiles of saline underflows and turbidity currents flowing over a mobile bed. J. Hydraul. Eng. 136, 412–433. http://dx.doi.org/10.1061/(ASCE)HY.1943-7900.0000200.

Stacey, M.W., Bowen, A.J., 1988. The vertical structure of density and turbidity currents: Theory and observations. J. Geophys. Res.: Ocean. 93, 3543–3553. http://dx.doi.org/10.1029/JC093iC04p03543.

Stecca, G., Siviglia, A., Blom, A., 2014. Mathematical analysis of the Saint-Venant-Hirano model for mixed-sediment morphodynamics. Water Resour. Res. 50, 7563–7589. http://dx.doi.org/10.1002/2014WR015251.

Stokes, G.G., 1851. On the effect of the internal friction of fluids on the motion of pendulums. Trans. Camb. Philos. Soc. 9, 8–94.

Sumner, E.J., Amy, L.A., Talling, P.J., 2008. Deposit structure and processes of sand deposition from decelerating sediment suspensions. J. Sediment. Res. 78, 529–547. http://dx.doi.org/10.2110/jsr.2008.062.

Sylvester, Z., Lowe, D.R., 2004. Textural trends in turbidites and slurry beds from the Oligocene flysch of the East Carpathians, Romania. Sedimentology 51, 945–972. http://dx.doi.org/10.1111/j.1365-3091.2004.00653.x.

Talling, P.J., Baker, M.L., Pope, E.L., Ruffell, S.C., Jacinto, R.S., Heijnen, M.S., Hage, S., Simmons, S.M., Hasenhündl, M., Heerema, C.J., McGhee, C., Apprioual, R., Ferrant, A., Cartigny, M.J.B., Parsons, D.R., Clare, M.A., Tshimanga, R.M., Trigg, M.A., Cula, C.A., Faria, R., Gaillot, A., Bola, G., Wallance, D., Griffiths, A., Nunny, R., Urlaub, M., Peirce, C., Burnett, R., Neasham, J., Hilton, R.J., 2022. Longest sediment flows yet measured show how major rivers connect efficiently to deep sea. Nat. Commun. 13, 4193. http://dx.doi.org/10.1038/s41467-022-31689-3.

Talling, P.J., Hage, S., Baker, M.L., Bianchi, T.S., Hilton, R.G., Maier, K.L., 2023. The global turbidity current pump and its implications for organic carbon cycling. Annu. Rev. Mar. Sci. 16, 105–133. http://dx.doi.org/10.1146/annurev-marine-032223-103626.

Tang, X.Q., Koh, C.G., Luo, M., 2023. Numerical simulation of turbidity currents using consistent particle method. Adv. Water Resour. 180, 104536. http://dx.doi.org/10.1016/j.advwatres.2023.104536.

van Rijn, L.C., 1993. Principles of Sediment Transport in Rivers, Estuaries and Coastal Seas. Aqua Publications, Amsterdam.

Verboom, G.K., Slob, A., 1984. Weakly-reflective boundary conditions for two-dimensional shallow water flow problems. Adv. Water Resour. 7, 192–197. http://dx.doi.org/10.1016/0309-1708(84)90018-6.

Weimer, P., Link, M.H., 1991. Global petroleum occurrences in submarine fans and turbidite systems. In: Seismic Facies and Sedimentary Processes of Submarine Fans and Turbidite Systems. Springer US, pp. 9–67. http://dx.doi.org/10.1007/978-1-4684-8276-8_2.

Xu, J.P., Noble, M.A., Rosenfeld, L.K., 2004. In-situ measurements of velocity structure within turbidity currents. Geophys. Res. Lett. 31, L09311. http://dx.doi.org/10.1029/2004GL019718.